THE ASTROPHYSICAL JOURNAL, 954:41 (19pp), 2023 September 1

https://doi.org/10.3847/1538-4357/ace7d1

© 2023. The Author(s). Published by the American Astronomical Society.

OPEN ACCESS

CrossMark

How Large Is a Disk—What Do Protoplanetary Disk Gas Sizes Really Mean?

Leon Trapman[1] , Giovanni Rosotti[2,3,4] , Ke Zhang[1] , and Benoît Tabone[4,5]
[1] Department of Astronomy, University of Wisconsin-Madison, 475 N Charter St, Madison, WI 53706, USA; ltrapman@wisc.edu
[2] Dipartimento di Fisica, Università degli Studi di Milano, Via Giovanni Celoria, 16, I-20133 Milano, Italy
[3] School of Physics and Astronomy, University of Leicester, Leicester, LE1 7RH, UK
[4] Leiden Observatory, Leiden University, 2300 RA Leiden, The Netherlands
[5] Université Paris-Saclay, CNRS, Institut d'Astrophysique Spatiale, F-91405 Orsay, France
Received 2023 May 15; revised 2023 July 10; accepted 2023 July 12; published 2023 August 22

Abstract

It remains unclear what mechanism is driving the evolution of protoplanetary disks. Direct detection of the main candidates, either turbulence driven by magnetorotational instabilities or magnetohydrodynamical disk winds, has proven difficult, leaving the time evolution of the disk size as one of the most promising observables able to differentiate between these two mechanisms. But to do so successfully, we need to understand what the observed gas disk size actually traces. We studied the relation between $R_{CO,90\%}$, the radius that encloses 90% of the ^{12}CO flux, and R_c, the radius that encodes the physical disk size, in order to provide simple prescriptions for conversions between these two sizes. For an extensive grid of thermochemical models, we calculate $R_{CO,90\%}$ from synthetic observations and relate properties measured at this radius, such as the gas column density, to bulk disk properties, such as R_c and the disk mass M_{disk}. We found an empirical correlation between the gas column density at $R_{CO,90\%}$ and disk mass: $N_{gas}(R_{CO,90\%}) \approx 3.73 \times 10^{21}(M_{disk}/M_\odot)^{0.34}$ cm^{-2}. Using this correlation we derive an analytical prescription of $R_{CO,90\%}$ that only depends on R_c and M_{disk}. We derive R_c for disks in Lupus, Upper Sco, Taurus, and the DSHARP sample, finding that disks in the older Upper Sco region are significantly smaller ($\langle R_c \rangle = 4.8$ au) than disks in the younger Lupus and Taurus regions ($\langle R_c \rangle = 19.8$ and 20.9 au, respectively). This temporal decrease in R_c goes against predictions of both viscous and wind-driven evolution, but could be a sign of significant external photoevaporation truncating disks in Upper Sco.

Unified Astronomy Thesaurus concepts: Protoplanetary disks (1300); Astrochemistry (75)

1. Introduction

Protoplanetary disks are the birth sites of planets, and only by understanding disks and their properties can we understand planet formation (e.g., Morbidelli & Raymond 2016).

Among the disk properties, size is one of the most fundamental. On a simple level, in combination with the disk mass, disk size is the main parameter determining the disk surface density, which in turn represent the available material to be accreted into planets. On a perhaps deeper level, the evolution of the size can inform us on the mechanism driving disk evolution. For example, in a scenario in which accretion is driven by viscosity, the disk size needs to get larger with time (Lynden-Bell & Pringle 1974; Hartmann et al. 1998) in order to conserve the disk angular momentum: this is normally called viscous spreading. Conversely, if angular momentum is extracted by MHD winds, expansion is not required (Armitage et al. 2013; Bai 2016; Tabone et al. 2022; although see Yang & Bai 2021 for the possibility of wind-driven disks growing over time). It is worth mentioning that both processes could affect different parts of the disk simultaneously, thereby complicating our simple view of disk evolution (e.g., Alessi & Pudritz 2022). Other mechanisms such as the presence of a stellar companion (e.g., Papaloizou & Pringle 1977; Artymowicz & Lubow 1994; Rosotti & Clarke 2018; Zagaria et al. 2021, 2023b), external photoevaporation (e.g., Clarke 2007; Facchini et al. 2016; Haworth et al. 2018; Sellek et al. 2020; Winter &

Haworth 2022), and, if the disk size is determined from the dust continuum emission at submillimeter wavelengths, radial drift (Weidenschilling 1977; Rosotti et al. 2019) can reduce the size of a protoplanetary disk and make it smaller with time, which has important consequences for disk evolution.

In the previous discussion we have been purposely negligent in describing in detail what "size" means. The underlying assumption in the way the term is normally used is that the disk size should somehow reflect where the disk mass is distributed. In practice, since following the analytical solutions of Lynden-Bell & Pringle (1974) it is common to parameterize disk surface densities using an exponentially tapered power law, disk size is often intended as the scale radius of the exponential, normally denoted with R_c. Any other parameterization of the surface density can always be characterized by defining the radius enclosing a given fraction of the disk mass.

In observations, however, protoplanetary disks have multiple "sizes," and one has to be careful which size is being considered for any analysis to be meaningful. Sizes are different first of all because protoplanetary disks can be observed at multiple wavelengths and in multiple tracers. Before the Atacama Large Millimeter/submillimeter Array (ALMA) became available, most available measurements of disk sizes were done in the continuum at submillimeter wavelengths (see the review of pre-ALMA results by Williams & Cieza 2011), with measurements available also at optical wavelength thanks to the Hubble Space Telescope (Vicente & Alves 2005), although predominantly for objects in Orion. While ALMA greatly expanded the sample of submillimeter continuum disk sizes (e.g., Andrews et al. 2018; Hendler et al. 2020; Tazzari et al. 2021; Manara et al. 2023), one of ALMA's

Original content from this work may be used under the terms of the Creative Commons Attribution 4.0 licence. Any further distribution of this work must maintain attribution to the author(s) and the title of the work, journal citation and DOI.

biggest contributions is that we now have relatively large samples with measurements of gas sizes (Ansdell et al. 2017; Barenfeld et al. 2017; Sanchis et al. 2021; Long et al. 2022). We should highlight however that also "gas" is a generic term since many different gas-phase species are known in protoplanetary disks. In this paper with "gas" disk size we always mean its most abundant species, CO, and particularly its most abundant isotopologue, ^{12}CO. This choice is motivated by the fact that by far ^{12}CO, in virtue of its brightness, is the tracer with the largest observational sample of measured disk sizes.

Even once the wavelength and tracer are specified, one still needs to specify how the disk size is exactly determined from the observations; e.g., see Tripathi et al. (2017) for a discussion concerning the continuum. In this paper we will consider as the observational disk size the radius enclosing a given fraction of the total flux, since this definition is generic enough to be applied to any observation, and following common observational conventions, we take the fraction to be 90%. We denote this radius as $R_{\mathrm{CO},90\%}$.

Regardless of the observational tracer, one should stress that no available tracer is really tracing the disk size in the purely theoretical sense, i.e., these tracers tell us the surface brightness distribution of the given tracer, and not how the mass of the disk is distributed. This is because of several reasons: the abundance of the chosen tracer may vary throughout, the intensity can get weaker or stronger as the disk temperature varies, and the given tracer may not be optically thin, implying that its surface brightness does not trace its surface density. Investigating the link between the observed size ($R_{\mathrm{CO},90\%}$) of a protoplanetary disk and the theoretical size (R_c) is the purpose of this paper.

In order to accomplish this goal, we have run a grid of thermochemical models where we compute the abundance of ^{12}CO in the disk and we have ray-traced the models to account for radiative transfer effects. Starting from earlier work presented in Trapman et al. (2022a) and Toci et al. (2023), we then use this grid to derive simple, yet accurate, analytical relations which allow us to predict the observed disk size for a given disk mass and theoretical size. The benefit of an analytical relation is that it can be inverted relatively easily. We make use of this to derive R_c from observations of $R_{\mathrm{CO},90\%}$ of disks in Lupus and Upper Sco, and discuss the implications for disk evolution.

The paper is structured as follows. We first present the technical details of our models in Section 2, and then show our results concerning the relation between R_c and $R_{\mathrm{CO},90\%}$ in Section 3. In Section 4 we apply the inverse relation to measure R_c in an observational sample and discuss the caveats of our work, before finally drawing our conclusions in Section 5.

2. The `DALI` Models

The location of $R_{\mathrm{CO},90\%}$, defined as the radius that encloses 90% of the ^{12}CO 2–1 flux, depends on the CO emission profile, which in turn depends on the CO chemistry and thermal structure of the disk, both of which can be obtained using a thermochemical model. In this work we use the thermochemical code `DALI` (Bruderer et al. 2012; Bruderer 2013) to run a series of disk models. `DALI` self-consistently calculates the thermal and chemical structure of a disk with a given (gas and dust) density structure and stellar radiation field. The code first computes the internal radiation field and dust temperature structure using a 2D Monte Carlo method to solve the radiative

transfer equation. It then iteratively solves the time-dependent chemistry, calculates molecular and atomic excitation levels, and computes the gas temperature by balancing heating and cooling processes until a self-consistent solution is found. Finally, the model is ray-traced to construct synthetic emission maps. A more detailed description of the code is provided in Appendix A of Bruderer et al. (2012).

For the surface density profile of our models we take the self-similar solution of the generalized, i.e., viscous and/or wind-driven, disk evolution given in Tabone et al. (2022), which is a tapered power law of the form

$$\Sigma_{\mathrm{gas}}(R) = \Gamma\left(\frac{\xi + 2 - \gamma}{2 - \gamma}\right)\frac{M_{\mathrm{disk}}}{2\pi R_c^2}\left(\frac{R}{R_c}\right)^{-\gamma+\xi}$$
$$\times \exp\left[-\left(\frac{R}{R_c}\right)^{2-\gamma}\right]. \tag{1}$$

Here M_{disk} is the mass of the disk, R_c is the characteristic size, and γ is the slope of the surface density, which is related to the slope of $\tilde{\alpha}$ (see Tabone et al. 2022). For the viscous case γ coincides with the slope of the kinetic viscosity (see, e.g., Lynden-Bell & Pringle 1974). ξ is the mass ejection index (Ferreira & Pelletier 1995; Ferreira 1997) and Γ is the gamma function, which for common ranges of γ and ξ is a factor of order unity. In this work we will set $\xi = 0.25$, which is equivalent with only vertical angular momentum transport by an MHD wind. Note that ξ has only a small effect on $R_{\mathrm{CO},90\%}$ as shown in Figure 11 in Trapman et al. (2022a). Similarly we set $\gamma = 1$ for most of this work, but see in Section 3.2 for the effect of γ on our results. Note that in contrast to Trapman et al. (2020, 2022a) disk evolution is not included and the surface density is fixed for each model.

The vertical density is assumed to be a Gaussian around disk midplane, which is the outcome of hydrostatic equilibrium under the simplifying assumption that the disk is vertically isothermal (see Equation (A5)). To simulate the effect of observed disk flaring (e.g., Dullemond & Dominik 2004; Avenhaus et al. 2018; Law et al. 2021b, 2022), the vertical scale height of the disk is described by a power law as

$$H(R) = Rh_c\left(\frac{R}{R_c}\right)^{\psi}, \tag{2}$$

where h_c is the opening angle at R_c and ψ is the flaring angle.

Dust is included in the form of a two-dust population, following, for example, Andrews et al. (2011). Small grains (0.005–1 μm), making up a fraction $(1 - f_{\mathrm{large}})$ of the total dust mass are distributed over the full vertical and radial extent of the disk, following the gas. Large grains (1–10^3 μm) that make up the remaining f_{large} fraction of the dust mass have the same radial distribution as the gas, but are vertically confined to the midplane to simulate the effect of vertical dust settling. This is achieved by reducing their scale height by a factor $\chi < 1$.

Finally, the star is assumed to be a 4000 K blackbody with a stellar radius chosen such that the star has a stellar luminosity $L_* = 0.28\,L_\odot$. To this spectrum we add a 10^4 K blackbody to simulate the accretion luminosity released by a $10^{-8}\,M_\odot$ yr^{-1} stellar mass accretion flow, where we assume that 50% of the gravitational potential energy is released as radiation (e.g., Kama et al. 2015). Table 1 summarizes the parameters of our fiducial models.

Table 1
Fiducial DALI Model Parameters

Parameter	Range
Chemistry[a]	
Chemical age	1 Myr
[C]/[H][a]	1.35×10^{-4}
[O]/[H]	2.88×10^{-4}
Physical structure	
γ	[0.5, **1.0**, 1.5]
ξ	0.25
ψ	[0.05, **0.15**, 0.25]
h_c	[**0.1**, 0.2]
R_c	[5, 20, 40, **65**] au
$M_{\rm gas}$	$5 \times 10^{-7} - 10^{-1} \ M_\odot$
Gas-to-dust ratio	100
Dust properties	
$f_{\rm large}$	[0.8, **0.9**, 0.99]
χ	[0.1, **0.2**, 0.4]
Composition	Standard ISM[b]
Stellar spectrum	
$T_{\rm eff}$	4000 K + Accretion UV
L_*	[0.1, **0.28**, 1.0, 3.0] $L_\odot$
$\zeta_{\rm cr}$	$10^{-17} \ {\rm s}^{-1}$
Observational geometry	
i	0°
PA	0°
d	150 pc

Notes.
[a] We assume typical interstellar medium (ISM) abundances for the total carbon and oxygen abundances (Cardelli et al. 1996; Jonkheid et al. 2007; Woitke et al. 2009; Bruderer et al. 2012).
[b] Weingartner & Draine (2001); see also Section 2.5 in Facchini et al. (2017). Parameters shown in bold are varied in Section 3.2.

To test the empirical correlation presented in the next section we also ran multiple sets of models that, similar to our fiducial models, span a range of disk masses but where one of the fiducial model parameters was varied over two or more values. The selected parameters are all expected to have a significant effect on the gas density, the temperature structure, and/or the chemistry of CO. These model parameters include the stellar luminosity L_*, the opening angle h_c, the external interstellar radiation field (ISRF; i.e., UV field), the characteristic radius R_c, the slope of the surface density γ, the flaring angle ψ, the dust settling parameter χ, and the fraction of large grains $f_{\rm large}$. Further parameters such as, for example, the UV luminosity of the star, were also examined, but tests showed that they had no significant effect on $R_{\rm CO,90\%}$. The inclination of the disk can also affect $R_{\rm CO,90\%}$, but its effects can be minimized for moderately inclined disks ($<60°$) by measuring $R_{\rm CO,90\%}$ in the deprojected disk frame (see, e.g., Appendix A in Trapman et al. 2019).

3. Results

3.1. A Tight Empirical Correlation between $N_{gas}(R_{CO,90\%})$ and the Disk Mass

It is common practice to measure the protoplanetary gas disk sizes from the extent of the submillimeter ^{12}CO rotational emission. These low J lines require a relatively small column to become optically thick, allowing us to detect the low density material found in the outer part of the disk easily. Furthermore, at low column densities UV photons are able to photodissociate

CO, thus removing the molecule from the gas. The exact CO column density required to self-shield against this depends somewhat on the molecular hydrogen column and the temperature, but it lies at around a few times $10^{15} \ {\rm cm}^{-2}$ (see, e.g., van Dishoeck & Black 1988). Back-of-the-envelope calculations show that the radius where the CO millimeter lines become optically thin ($R_{\tau[\rm mm]=1}$) approximately coincides with the radius where it stops being able to self-shield against photodissociation ($R_{\rm CO \ p.d.}$). It should be noted that CO is also partly protected by mutual line shielding of CO by H_2, but this is negligible compared to the effect of CO self-shielding (see, e.g., Lee & Herbst 1996). This sets the expectation of a link between the observed gas disk size $R_{\rm CO,90\%}$, which is linked to $R_{\tau=1}$, and the surface density, albeit indirectly, from $N_{\rm CO}(R_{\rm CO \ p.d.}) \approx 10^{15} \ {\rm cm}^{-2}$ (see, e.g., Trapman et al. 2022a; Toci et al. 2023).

Using our thermochemical models, we can test this expectation. After measuring $R_{\rm CO,90\%}$ from the synthetic CO 2–1 observations of our models we find a surprisingly tight correlation between the gas column density[6] at the observed outer radius ($N_{\rm gas}(R_{\rm CO,90\%})$) and the mass of the disk ($M_{\rm disk}$). The top-left panel of Figure 1 shows that $N_{\rm gas}(R_{\rm CO,90\%})$ increases with $M_{\rm disk}$ as a power law, $N_{\rm gas}(R_{\rm CO,90\%}) \propto M_{\rm disk}^{0.34}$.

The positive correlation can be understood, at least qualitatively, by looking at the other quantities shown in Figure 1 that are also obtained at $R_{\rm CO,90\%}$. First off, the column density of CO at $R_{\rm CO,90\%}$, denoted as $N_{\rm CO}(R_{\rm CO,90\%})$, has an approximately constant value of $\approx 2 \times 10^{15} \ {\rm cm}^{-2}$ across the full disk mass range examined here. This value corresponds to the CO column required for CO self-shielding (e.g., van Dishoeck & Black 1988), which matches with the expectation discussed earlier that $R_{\rm CO,90\%}$ roughly coincides with the radius where CO starts to become photodissociated. We would therefore expect that the observed disk size $R_{\rm CO,90\%}$ increases with disk mass, because this critical CO column density, assuming a fixed CO abundance, lies further out for a disk that has more mass (see, e.g., Trapman et al. 2020). However, further out from the star the disk is also colder and a larger fraction of the CO column is frozen out, resulting in a lower column-averaged CO abundance. This is corroborated by the rightmost panels of Figure 1, which show that the column-averaged CO abundance decreases for higher disk masses and that the height below which CO freezes out increases with disk mass. This decreasing CO abundance means that the gas column density at $R_{\rm CO,90\%}$ needs to increase with disk mass in order to reach the same constant CO column density.

While this empirical correlation is evident in the models and can be understood qualitatively, it is difficult to reproduce quantitatively. Appendix A shows how this could be done using a toy model. It also shows that $R_{\tau_{\rm CO} = 1}$, the radius where ^{12}CO 2–1 becomes optically thin, is the more logical choice for such a model, rather than $R_{\rm CO,90\%}$. However, while this toy model is able to show a correlation between $N_{\rm gas}(R_{\tau_{\rm CO} = 1})$ and $M_{\rm disk}$, in practice the empirical relation between $N_{\rm gas}(R_{\rm CO,90\%})$ and $M_{\rm disk}$ shown in Figure 1 provides a much tighter correlation. In light of this we will use this empirical correlation throughout the rest of this work.

---

[6] In this work the gas column density is defined assuming a mean molecular weight $\mu = 2.3$, so $N_{\rm gas} = \frac{\Sigma_{\rm gas}}{2.3 m_H}$.
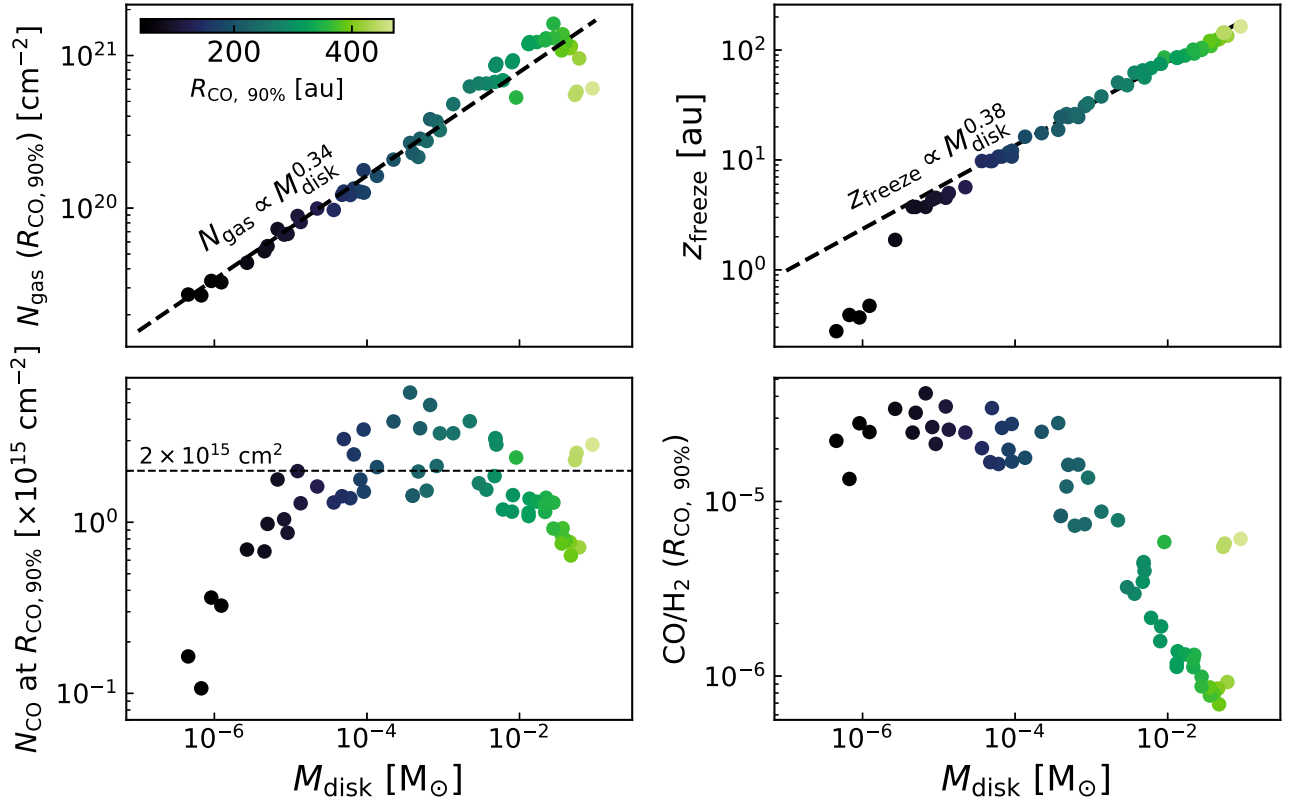
Figure 1. Properties measured at $R_{CO,90\%}$ from DALI models with $R_c = 65$ au and $M_{disk} = (10^{-7} - 10^{-1}\,M_\odot)$. Top left: gas column density at $R_{CO,90\%}$ against the disk mass. Colors show the $R_{CO,90\%}$ of the disk. The black dashed line shows the correlation between $N_{gas}(R_{CO,90\%})$ and M_{disk}. Top right: the height of the CO freeze-out layer at $R_{CO,90\%}$ vs. the disk mass. The black dashed line shows the correlation between $z_{freeze}(R_{CO,90\%})$ and M_{disk}, similar to the one seen in the top-left panel. Bottom left: CO column density at $R_{CO,90\%}$ vs. the disk mass. Bottom right: column-averaged CO abundance (i.e., $N_{CO}(R_{CO,90\%})/N_{gas}(R_{CO,90\%})$) at $R_{CO,90\%}$ vs. disk mass.

3.2. Robustness of the Correlation against Varying Disk Parameters

Figure 2 shows that the correlation between $(N_{CO}(R_{CO,90\%}))$ and M_{disk} not only shows up for a single set of models but is unaffected by most disk parameters. The exceptions are the stellar luminosity, the strength of the external ISRF and the slope of the surface density profile. The stellar luminosity directly affects the temperature structure of disk. Increasing it moves the CO snow surface closer to the midplane. This increases the column-averaged CO column at $R_{CO,90\%}$, which reduces the gas column needed to obtain the critical CO column density.

Increasing the ISRF has two effects on the location of $R_{CO,90\%}$. First, a larger CO column, and therefore also a larger gas column, is required to self-shield the CO against the stronger UV radiation field. Second, the external radiation will heat up the gas in the outer disk, which can thermally desorb CO ice back into the gas. This will increase the column-averaged CO abundance, moving $N_{gas}(R_{CO,90\%})$ down again. The latter effect likely explains why for a high disk mass both sets of models coincide again in Figure 2.

Finally, models with a steeper surface density slope ($\gamma = 1.5$) have a much shallower exponential taper in the outer disk ($\Sigma_{gas,outer} \propto \exp[-(R/R_c)^{2-\gamma}]$). Depending on the mass of the disk the CO emission in this taper can be partially optically thin. Inspection of the models shows that ones with $\gamma = 0.5-1$ have $\tau \gtrsim 1$ at $R_{CO,90\%}$, whereas models with $\gamma = 1.5$ have $\tau \approx 0.1$ at this radius. The presence of significant optically thin CO emission means $R_{CO,90\%}$ no longer directly traces the radius where CO stops being able to self-shield. This is an important

reason why $N_{gas}(R_{CO,90\%})$ scales with M_{disk} (see Appendix A for details).

3.3. Deriving an Analytical Expression for $R_{CO,90\%}$

If we fit the models presented in the previous section with a simple power law between the gas column density at $R_{CO,90\%}$ and the disk mass, we obtain

$$N_{gas}(R_{CO,90\%}) \equiv N_{gas,crit} \approx 3.7 \times 10^{21} \left(\frac{M_{gas}}{M_\odot}\right)^{0.34} \text{cm}^{-2}. \quad (3)$$

As discussed in the previous section, most disk parameters do not affect this power law. Of the ones that do, only the stellar luminosity dependence can be readily included, as it only changes the slope and normalization of the power law by a small factor. If we fit the stellar luminosity dependence of these two parts of our power law, we obtain

$$N_{gas,crit} \approx 10^{21.27 - 0.53\log_{10} L_*} \left(\frac{M_{gas}}{M_\odot}\right)^{0.3 - 0.08\log_{10} L_*} \text{cm}^{-2}. \quad (4)$$

As showed in the recent work by Toci et al. (2023) we can use this critical gas column density to obtain an analytical expression for $R_{CO,90\%}$. While Toci et al. (2023) left this critical value as a free parameter (Σ_{crit} in their notation), our models provide a quantitative estimate for this parameter.

Because the analytical solution contains a special function, Lambert W-function or product-log function, it is convenient to consider the case in which $R_{CO,90\%} \gg R_c$, i.e., that $R_{CO,90\%}$ lies far into the exponential taper of the surface density profile. This

case is more traceable and it is straightforward to show from Equations (1) and (3) that the observed outer radius scales with the logarithm of the disk mass as

$$\frac{\mu m_H N_{\text{gas,crit}}}{\Sigma_c} \approx \exp\left[-\left(\frac{R_{\text{CO,90\%}}}{R_c}\right)^{2-\gamma}\right], \qquad (5)$$

$$R_{\text{CO,90\%}} \overset{\gamma=1}{\approx} R_c[0.66 \ln M_{\text{disk}} - 2 \ln R_c + const], \qquad (6)$$

where M_{disk} and R_c are in units of $M_\odot$ and au, respectively.

To first order the observed outer radius is thus expected to scale with the logarithm of the disk mass. Its dependence on R_c is more complex and will be explored in the next section.

If the surface density profile (Equation (1)) is inverted without any simplifying assumptions we obtain the following analytical prescription for $R_{\text{CO,90\%}}$ as function of M_{disk}, R_c (and L_*)[7]

$$R_{\text{CO,90\%}}$$
$$= R_c\left(\frac{\gamma-\xi}{2-\gamma}W\left(\frac{2-\gamma}{\gamma-\xi}\left[4.9 \cdot 10^7\left(\frac{M_d}{M_\odot}\right)^{0.66}\left(\frac{\text{au}}{R_c}\right)^2\right]^{\frac{2-\gamma}{\gamma-\xi}}\right)\right)^{\frac{1}{2-\gamma}}. \qquad (8)$$

Here $W(z)$ is the Lambert W-function, or product-log function, specifically its principal solution ($k=0$).

For common assumptions of a viscously evolving disk, i.e., $\gamma = 1$ and $\xi = 0$, the prescription reduces to

$$R_{\text{CO,90\%}} = R_c \times W\left(\left[4.9 \times 10^7\left(\frac{M_{\text{disk}}}{M_\odot}\right)^{0.66}\left(\frac{R_c}{1\text{ au}}\right)^{-2}\right]\right). \qquad (9)$$

Similarly, for $\gamma = 1$ and $\xi = 0.25$ (the values of the fiducial models in this work),

$$R_{\text{CO,90\%}}$$
$$= \frac{3R_c}{4} \times W\left(\frac{4}{3}\left[4.9 \times 10^7\left(\frac{M_{\text{disk}}}{M_\odot}\right)^{0.66}\left(\frac{R_c}{1\text{ au}}\right)^{-2}\right]^{\frac{4}{3}}\right). \qquad (10)$$

Equation (8) allows us to calculate $R_{\text{CO,90\%}}$ analytically from just R_c, M_{disk}, L_*, and the slope of the surface density. Before we use it, however, it is worthwhile to examine how well it reproduces the $R_{\text{CO,90\%}}$ obtained from our disk models. Figure 3 shows this comparison for both the approximation that the dominant part of the surface density profile is its exponential taper (see Equation (5)) and for the full derivation of an analytical $R_{\text{CO,90\%}}$ (Equation (8)).

The approximation of the surface density as just its exponential taper, as was proposed in, for example, Trapman et al. (2022a), captures the general trend of $R_{\text{CO,90\%}}$ increasing with M_{disk}, but does not match the exact shape of the mass dependence of $R_{\text{CO,90\%}}$. The $R_{\text{CO,90\%}}$ calculated using Equation (8) greatly improves the match, showing excellent agreement with the $R_{\text{CO,90\%}}$ obtained from the disk models.

---

[7] Note that if the stellar luminosity dependence of $N_{\text{gas,crit}}$ is included, the term in the square brackets of Equations (8), (9), and (10) becomes

$$[..] = 9.862 \times 10^{7+0.53\log_{10}L_*}\left(\frac{M_d}{M_\odot}\right)^{0.70+0.08\log_{10}L_*}\left(\frac{R_c}{\text{au}}\right)^{-2}, \qquad (7)$$

where L_* is in units of $L_\odot$.

Only for the very lowest and highest disk masses do we see a significant difference between the models and the analytical $R_{\text{CO,90\%}}$. Note that these are the same models where $N_{\text{gas}}(R_{\text{CO,90\%}})$ does not follow the power-law relation with M_{disk} (see Figure 1).

Figure 3 also shows the equivalent of the expression for $R_{\text{CO,90\%}}$ presented by Toci et al. (2023), who derive $R_{\text{CO,90\%}}$ from where the surface density reaches a critical value $\Sigma_{\text{crit}} = \xi_{\text{CO}}^{-1} 2 m_H \hat{N}_{\text{CO}}$. The line shown here is for their adopted best values, $\xi_{\text{CO}} = 10^{-6}$ and $\hat{N}_{\text{CO}} = 10^{16}$ cm^{-2}. Around a disk mass of $M_{\text{gas}} \approx 10^{-2}-10^{-1} M_\odot$ both the models and the analytical expression for $R_{\text{CO,90\%}}$ from this work agree well. In their work, Toci et al. (2023) use a fiducial initial disk mass of $0.1 M_\odot$ and evaluate the viscous evolution of $R_{\text{CO,90\%}}$ between 0.1 and 3 Myr. Given the fact the mass of viscously evolving disks only decreases slowly over time ($M_{\text{disk}} \propto^{-0.5}$ for $\gamma = 1$) the disk masses covered in their work mostly lie in the $M_{\text{disk}} \approx 10^{-2}-10^{-1} M_\odot$ range where the models and the analytical expressions all agree.

3.4. The Link between $R_{CO,90\%}$ and R_c

Up to this point we have computed the observed radius $R_{\text{CO,90\%}}$ for models where R_c was given. Observationally, however, we are interested in solving the opposite problem: for a given $R_{\text{CO,90\%}}$ that was obtained from observations, what is the corresponding R_c? To that end, having vetted Equation (8) using our DALI models, we can now use it to study the relation between $R_{\text{CO,90\%}}$ and R_c in disks. Figure 4 shows $R_{\text{CO,90\%}}$ as a function of R_c for four different disk masses using $\gamma = 1$ and $\xi = 0.25$. The shape of the curve shows that there are two values of R_c that can be inferred from a measurement of $R_{\text{CO,90\%}}$. Figure 5 is a visualization of this, showing a set of example gas surface densities that all have the same total disk mass but a different R_c. Two profiles intersect with $N_{\text{gas}}(R_{\text{CO,90\%}})$ at $R_{\text{CO,90\%}}$: R_c=20 au and R_c=1000 au. The first R_c is much smaller than $R_{\text{CO,90\%}}$, meaning that $R_{\text{CO,90\%}}$ lies in the exponential taper, while the other R_c that is larger than $R_{\text{CO,90\%}}$ lies in the power-law part of the surface density. We should note however that while the "power-law R_c" is a mathematical solution for $R_{\text{CO,90\%}}$ it is also an extrapolation for Equation (8) beyond the domain where it was tested. None of the DALI models examined in this work have $R_c > R_{\text{CO,90\%}}$ and it is entirely possible that disks with such a disk structure, likely those with a very low disk mass, do not follow the $N_{\text{gas}}(R_{\text{CO,90\%}})-M_{\text{disk}}$ correlation on which Equation (8) is built.

Interestingly, the curves in Figure 4 also imply that for a given disk mass there is a maximum observed disk size, where $R_{\text{CO,90\%}}$ is equal to R_c. Increasing R_c beyond this point decreases $R_{\text{CO,90\%}}$ as a large fraction of the disk mass ($\gtrsim 50\%$, see the top panel of Figure 4) now exists as low-surface-density material below the CO photodissociation threshold. A demonstration of this effect can be seen in the evolution of $R_{\text{CO,90\%}}$ for a low-mass viscously evolving disk. As can be seen in, for example, Trapman et al. (2020, their Figure 3), the $R_{\text{CO,90\%}}$ of a low-mass, high-viscosity disk first increases with time until the rapid viscous expansion lowers the surface density to the point where the CO photodissociation front starts moving inward, resulting in $R_{\text{CO,90\%}}$ now decreasing with time.

The existence of a maximum $R_{\text{CO,90\%}}$ for each disk mass also suggests that $R_{\text{CO,90\%}}$ places a lower limit on the disk mass. By taking the derivative of $R_{\text{CO,90\%}}$ to R_c and setting it to zero, this minimum disk mass can be written as (for the
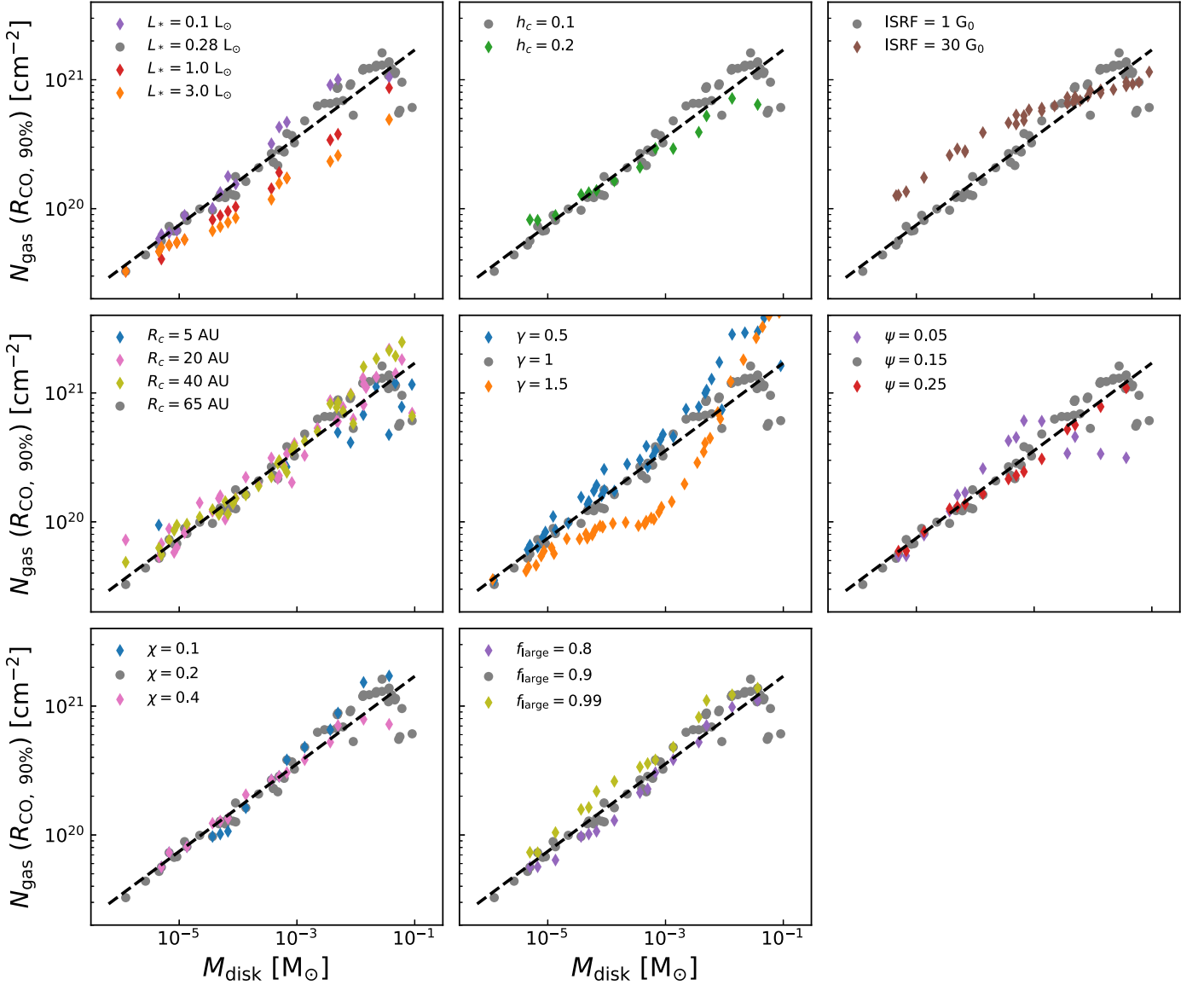
Figure 2. Correlation between $N_{gas}(R_{CO,90\%})$ and M_{disk} examined for a wide range of disk and stellar parameters. From left to right and top to bottom, the examined parameters are the stellar luminosity (L_*), the scale height at R_c (h_c), the external ISRF, the characteristic size (R_c), the slope of the surface density (γ), the disk flaring angle (ψ), the scale height reduction of the large grains (χ), and the fraction of large grains (f_{large}). The gray points in each panel show the fiducial models shown in Figure 1. The black dashed line shows $N_{gas}(R_{CO,90\%}) \propto M_{disk}^{0.34}$.

derivation, see Appendix D)

$$M_{disk} \gtrsim 1.3 \times 10^{-5} \left(\frac{R_{CO,90\%}}{100 \text{ au}} \right)^3 M_\odot. \qquad (11)$$

It should be kept in mind however that this disk mass has been derived by assuming a surface density profile and fitting it through a single point (N_{gas} at $R_{CO,90\%}$). Its accuracy therefore depends on how well this surface density profile matches the actual surface density of protoplanetary disks.

4. Discussion

4.1. Extracting an Estimate of R_c from Observed $R_{CO,90\%}$

In the previous section we showed that Equation (8) provides a link between $R_{CO,90\%}$ and R_c based on M_{disk}. Leveraging this equation we can derive R_c from the observed disk sizes that have now been measured from ^{12}CO emission for a large

number of disks distributed over several star-forming regions[8] (e.g., Barenfeld et al. 2017; Ansdell et al. 2018; Sanchis et al. 2021; Long et al. 2022; see Table 2 and Figure 6). Before we continue there are two things that should be kept in mind. The observations from which these sizes are measured are shallow, which means that the uncertainties on most $R_{CO,90\%}$ values are large, up to 30% (see Sanchis et al. 2021). Another good example of this is the observations of disks in Upper Sco, where Barenfeld et al. (2017) detected ^{12}CO 3–2 in 23 of the 51 continuum-detected sources, but from fitting the CO visibilities was only able to provide well-constrained gas disk sizes (i.e., statistically inconsistent with 0) for seven disks in the sample. So when deriving R_c we have to take the uncertainties on $R_{CO,90\%}$ into account.
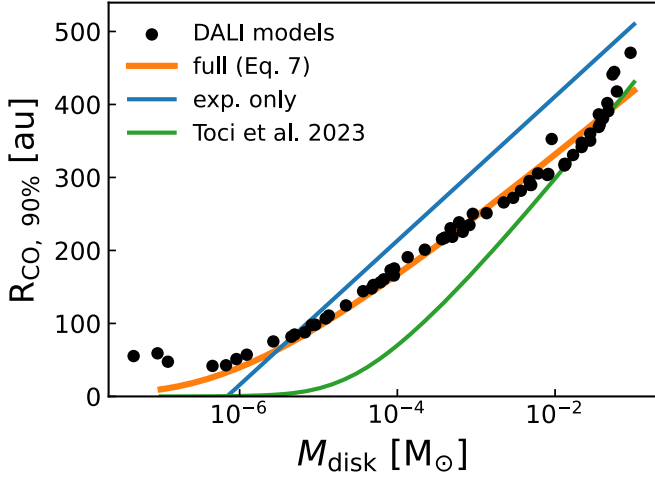

Figure 3. Comparison between the analytically calculated $R_{CO,90\%}$ and the one obtained from the models using the fiducial disk parameters given in Table 1. Black points show the model $R_{CO,90\%}$. The orange line shows $R_{CO,90\%}$ calculated using Equation (8). The blue line shows $R_{CO,90\%}$ calculated by approximating the surface density profile by its exponential taper (Equation (5)). The green line shows the equivalent of expression for $R_{CO,90\%}$ from Toci et al. (2023), see Section 3.3 for details.

Inverting Equation (8) also requires the disk gas mass, which is a difficult quantity to measure. Gas masses derived from CO isotopologue emission are found to be low ($\lesssim 1\ M_{Jup}$; see, e.g., Ansdell et al. 2016; Long et al. 2017; Miotello et al. 2017). However, there are large uncertainties on the CO abundance in disks (e.g., Favre et al. 2013; Schwarz et al. 2016; Zhang et al. 2019, 2020; Trapman et al. 2022b). We will therefore make the assumption that all disks have a gas-to-dust mass ratio of 100. For the disks where the gas mass is measured using hydrogen deuteride, the gas-to-dust mass ratio seems approximately 100, although this is only for a few disks in a very biased sample. New observations from the ALMA survey of Gas Evolution in Protoplanetary disks (AGE-PRO) will allow us to overcome this hurdle by measuring accurate gas masses for 20 disks in Lupus and Upper Sco, using N_2H^+ to constrain their CO abundance observationally (see Trapman et al. 2022b for details). We will discuss the assumption of a single gas-to-dust mass ratio later in this section.

The details for our approach of obtaining R_c from $R_{CO,90\%}$ can be found in Appendix E. Before continuing to the R_c distributions of our various samples, let us first examine the computed R_c for five well-known disks that have been previously studied in detail using thermochemical models that reproduce, among a number of other observables, the observed extent of CO and its isotopologues: TW Hya, DM Tau, IM Lup, AS 209, and GM Aur (Kama et al. 2016; Zhang et al. 2019; Schwarz et al. 2021; Zhang et al. 2021). For three of the five disks, DM Tau, IM Lup, and TW Hya, the simple estimate in Table 2 roughly agrees with the R_c in the more detailed studies. Not so for GM Aur and AS 209 however, which have estimated R_c values that are much smaller than the literature values. For AS 209, the difference in R_c can be traced back to the fact that the disk mass used here (i.e., $100 \times M_{dust}$) is $\sim 10\times$ larger than the one derived by Zhang et al. (2021). For GM Aur it is harder to identify a similar cause. It should be noted though that fitting R_c was not the primary goal of the previous studies discussed here. These detailed models reproduce the observations for the given R_c, but due to the
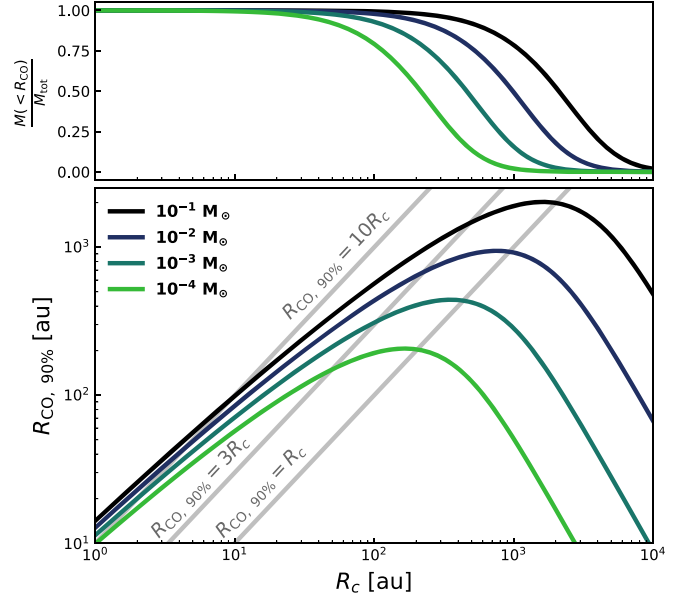

Figure 4. Bottom analytical $R_{CO,90\%}$ calculated using Equation (8) for a range of R_c. Colors show different disk masses. Top: fraction of the total disk mass that is within $R_{CO,90\%}$, corresponding the solid line in the bottom panel.
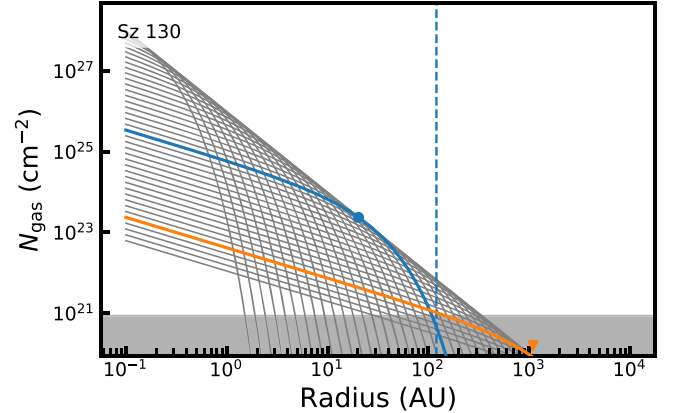
Figure 5. Gas surface density profiles calculated for different R_c but that all have the same total disk mass. The top of the gray shaded region shows the critical gas column density at $R_{CO,90\%}$ for this disk. The vertical dashed line shows the observed $R_{CO,90\%}$. Two profiles with different R_c (marked by colored symbols) have this column density at $R_{CO,90\%}$.

complexity of the fitting it is hard to determine how unique these values of R_c are.

To examine and compare the distributions of R_c in different star-forming regions, we sum up the distributions of R_c for individual sources in each region and normalize the resulting distribution. Figure 7 shows the normalized distribution of R_c for Lupus, Upper Sco, Taurus, and the DSHARP sample. Lupus and Taurus have similar median R_c, $19.8^{+12.8}_{-9}$ au and $20.9^{+54.4}_{-9.6}$ au for the two regions, respectively, while the DSHARP sample has a slightly larger median $R_c = 26.1^{+12.1}_{-9.7}$ au. Here the uncertainties denote the 25% and 75% quantiles of the distribution. The clear outlier is Upper Sco with a median $R_c = 4.9^{+4.4}_{-3.2}$. This is a surprising find given the age difference between Lupus/Taurus ($\sim$1–3 Myr; e.g., Comerón 2008) and Upper Sco ($\sim$5–11 Myr; e.g., Preibisch et al. 2002; Pecaut et al. 2012). Figure 7 thus shows a decrease in R_c with time, which
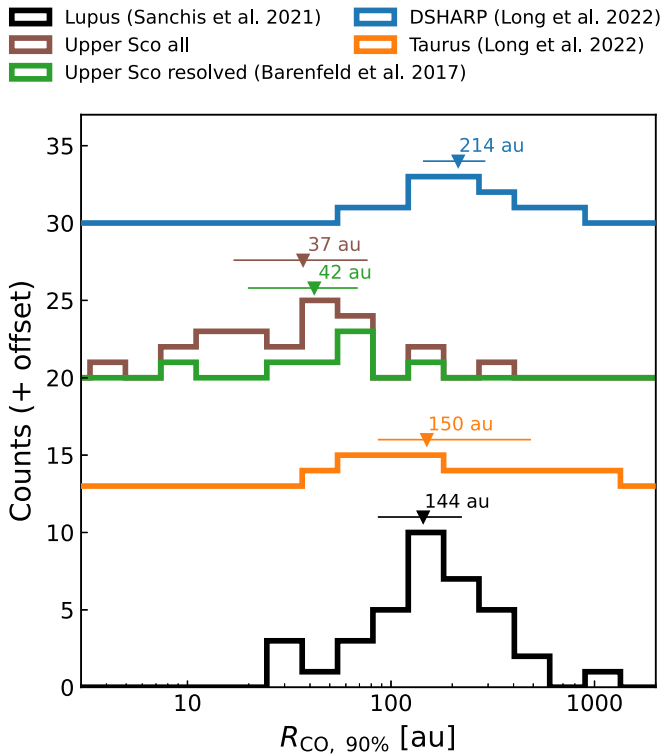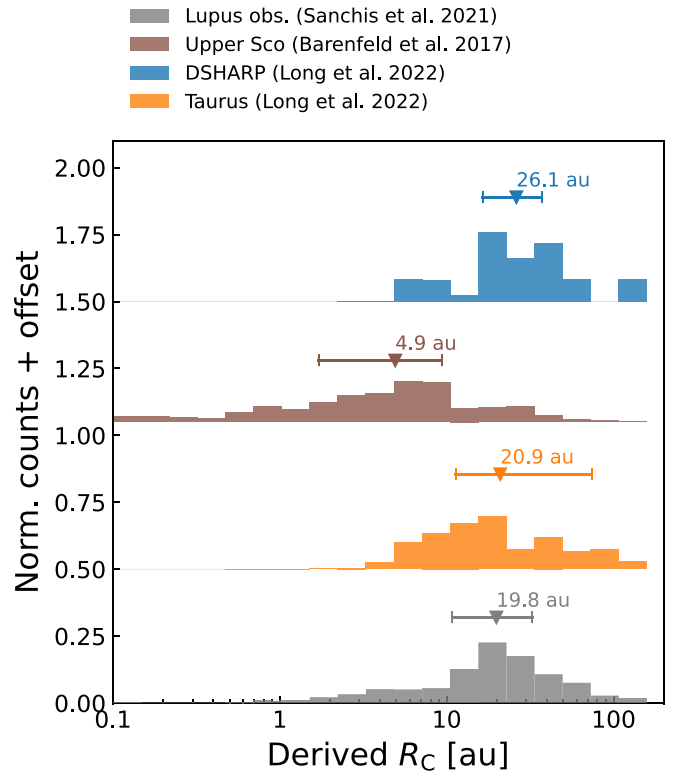
Figure 6. Distribution of observed disk sizes $R_{CO,90\%}$ for Lupus (black), Upper Sco (brown/green), Taurus (blue), and DSHARP (orange). The resolved Upper Sco sample shown here includes only the seven well-resolved sources, while the full sample includes all sources where ^{12}CO was detected (for details, see Barenfeld et al. 2017). The triangles denote the median $R_{CO,90\%}$ and the horizontal line shows the 25th and 75th quantiles of the $R_{CO,90\%}$ distribution of each region.

Figure 7. Derived distributions of R_c for four disk samples: Lupus (gray; Ansdell et al. 2018; Sanchis et al. 2021), Upper Sco (brown; Barenfeld et al. 2017), Taurus (orange; Long et al. 2022), and DSHARP (blue; Andrews et al. 2018; Long et al. 2022). The triangles denote the median R_c and the horizontal line shows the 25th and 75th quantiles of the R_c distribution of each region. See Table 2 for the R_c of individual disks.

does not match with predictions from either of the predominant theories of disk evolution. Viscously evolving disks are expected to grow over time, with R_c increasing with age. Conversely, disks evolving under the effect of MHD disks winds are expected to have an R_c that is constant with time. Even a combination of viscous and MHD wind-driven evolution would be hard pressed to explain the decrease of R_c, given the inability of both components to explain the observed decrease in R_c. A potential cause for the systematically smaller R_c in Upper Sco is the environment in which these disks find themselves, specifically their proximity to the nearby Sco–Cen OB association. UV radiation from these O- and B-stars could have truncated the disks (e.g., Facchini et al. 2016; Haworth et al. 2017, 2018; Winter et al. 2018), resulting in a different evolutionary path compared to the disks in the more quiescent Lupus and Taurus star-forming regions. Note that in the case of truncated disks the R_c values derived here for Upper Sco should be viewed with caution, as they are derived under the assumption of a tapered power-law surface density profile, an assumption which is no longer valid in this case. We reserve a more comprehensive analysis of the effect of external photoevaporation on $R_{CO,90\%}$ in Upper Sco for a future work.

4.2. Caveats and Limitations

When comparing the median R_c of different regions in Section 4.1 there are several factors that we should keep in mind. The first is that none of these samples are complete. Due to the limited sensitivity of the observations the faintest and most compact sources are likely not detected and thus not

included in the sample. The inclusion of these sources would decrease the median R_c if they are compact, but without deep observations we cannot rule out the existence of large, low-surface-brightness disks that would increase the median R_c.

Similarly, the binarity of the samples should be considered. Binaries can truncate the disk and, more generally, disks in multiple systems evolve differently than those around single stars (see, e.g., Kraus et al. 2012; Rosotti & Clarke 2018; Zagaria et al. 2021, 2022). Indeed, there is some suggestion that Upper Sco has a higher binary fraction than Lupus (e.g., Barenfeld et al. 2019; Zurlo et al. 2021; Zagaria et al. 2022). However, this should not be taken at face value, as our samples are not complete and the binarity surveys are not homogeneous (see Appendix A of Zagaria et al. 2021 for an extensive discussion on this). A homogenous study of disk multiplicity is needed to show its effect on disk sizes conclusively.

There is also a difference in methodology that needs to be considered. The $R_{CO,90\%}$ in Lupus, Taurus, and DSHARP were all measured from integrated intensity maps of CO emission. As mentioned above, the $R_{CO,90\%}$ values of Upper Sco are measured from a CO intensity profile that was fitted to the visibilities (see Barenfeld et al. 2017). It is possible that this introduces some systematic effect that results in lower values for R_c in Upper Sco. These observed $R_{CO,90\%}$ are then compared to the noiseless, high-resolution synthetic CO observations of our models, which are most akin to the DSHARP observations (see, e.g., Section 3.1.2 in Sanchis et al. 2021 for a detailed discussion how higher resolution and/ or sensitivity affect the measurement of $R_{CO,90\%}$). It is also worth pointing out that the Upper Sco gas disk sizes are

measured from the ^{12}CO $J = 3\text{–}2$ line rather than the $J = 2\text{–}1$ line used for the other regions, but models show that has only a small ($\lesssim 10\%$) effect on $R_{\mathrm{CO},90\%}$ (e.g., Trapman et al. 2019). The forthcoming AGE-PRO observations will test this possibility by consistently measuring gas disk sizes for a carefully selected sample of disks in Lupus and Upper Sco.

The assumption of a single gas-to-dust mass ratio for all sources irrespective of their age is also likely to be incorrect. Dust evolution models show that the gas-to-dust ratio increases with age as more of the dust mass is converted into larger bodies that either drift inward and are accreted onto the star (e.g., Birnstiel et al. 2012) or form planetesimals that do not emit at millimeter wavelengths and are thus unaccounted for in our dust masses (e.g., Pinilla et al. 2020). This would however only increase the difference between Upper Sco and the younger regions, as to explain the same $R_{\mathrm{CO},90\%}$ with a higher mass disk requires a smaller R_{c}. Using a lower gas-to-dust mass ratio for Upper Sco would move the median R_{c} closer to the values of Lupus and Taurus. However, Figure 4 shows that the effect of changing the disk mass is small. To produce an $R_{\mathrm{CO},90\%}$ of, for example, 60 au requires an R_{c} of ≈ 5 au if the disk has a mass of $M_{\mathrm{disk}} = 0.1\ M_{\odot}$, which increases to $R_{\mathrm{c}} \approx 10$ au for a disk that is three order of magnitude less massive ($M_{\mathrm{disk}} = 10^{-4}\ M_{\odot}$).

Another source of uncertainty is the global CO abundance in the disk. The processes that have been proposed for removing CO from the gas in disks (beyond CO freeze out and photodissociation) are expected to operate on megayear timescales (e.g., Yu et al. 2017; Bosman et al. 2018; Krijt et al. 2018, 2020), which is corroborated by observations (e.g., Zhang et al. 2020). In addition to differences between individual sources we can thus expect a trend of lower CO abundances with age. Observations of N_2H^+ of two disks in Upper Sco suggest that this is indeed the case (see Anderson et al. 2019). If the overall CO abundance in the disk is lower the gas column at $R_{\mathrm{CO},90\%}$ needs to be larger to build up a CO column capable of self-shielding against photodissociation. Given that the total disk mass is fixed the derived R_{c} will have to increase to explain the same $R_{\mathrm{CO},90\%}$ with a lower CO abundance.

Quantifying the effect on $R_{\mathrm{CO},90\%}$ depends on the exact physical and/or chemical processes responsible for removing the CO from the gas, but also, maybe even more importantly, on how well mixed the disk is vertically. If vertical mixing is inefficient CO could be removed from the midplane, as traced by ^{13}CO and C^{18}O, while the upper layers of the disk from which ^{12}CO emits remain unaffected. In this case, $R_{\mathrm{CO},90\%}$ would not be significantly affected by a decrease in CO abundance (see Trapman et al. 2020).

Conversely, if the disk is well mixed vertically the CO abundance in the ^{12}CO emitting layer will also lower than currently assumed. Trapman et al. (2022a) showed that this, coupled with the relatively poor brightness sensitivity of the shallow ALMA disk surveys, can significantly reduce the observed value of $R_{\mathrm{CO},90\%}$. Accounting for this fact would bring the characteristic radii of Upper Sco closer to those of disks in Lupus and Upper Sco. Recent work by Zagaria et al. (2023a) arrived at a similar conclusion. We should also note that the CO depletion factor is seen to vary with radius (Zhang et al. 2019, 2021), which complicates extrapolating the CO abundance of the bulk of the gas to the region in the outer disk that is most relevant for setting $R_{\mathrm{CO},90\%}$.

The shape of the surface density in the outer disk is an important part in the analytical relation between $R_{\mathrm{CO},90\%}$ and R_{c} presented in this work (see also Appendix A). Most notably, our models assume that the surface density follows an exponential taper. While this assumption is well grounded in theory, observational constraints on the surface density in the outer part of disks are sparse (e.g., Dullemond et al. 2020). Figure 2 gives us some idea about in what way the surface density must be different to nullify the $N_{\mathrm{gas}}(R_{\mathrm{CO},90\%})\text{–}M_{\mathrm{disk}}$ relation. If γ is decreased, in which case the exponential taper becomes steeper and the surface density starts to approach a truncated power law, the $N_{\mathrm{gas}}(R_{\mathrm{CO},90\%})\text{–}M_{\mathrm{disk}}$ relation is retained. This suggests that the relation should be there for disks where the surface density drops off steeply, whereas for disks with a shallow surface density profile in the outer disk the relation will no longer hold and the analytical expression for $R_{\mathrm{CO},90\%}$ should not be used. However, we should remain cautious when extrapolating from our "γ models." By construction, a steeper exponential taper (i.e., small γ) corresponds to a flatter power law at small radii and vice versa for large γ. In the end it is always prudent to use tailored models for disks with noticeably, or expected, different surface density profiles rather than use a generalized model. In a similar vein, substructures in the gas and radial variations in the gas-to-dust mass ratio could affect $R_{\mathrm{CO},90\%}$. However, as $R_{\mathrm{CO},90\%}$ is measured from the optically thick ^{12}CO emission these structures would need to change the temperature structure in the ^{12}CO emitting layer meaningfully to affect the ^{12}CO emission profile and therefore $R_{\mathrm{CO},90\%}$. Law et al. (2021a) showed that high-resolution ^{12}CO observations show comparatively little substructure in contrast to more optically thin CO isotopologues and the dust. However, if a substructure near $R_{\mathrm{CO},90\%}$ were to change the temperature structure locally and thereby change the location of the CO snow surface it would likely break the $N_{\mathrm{gas}}(R_{\mathrm{CO},90\%})\text{–}M_{\mathrm{disk}}$ correlation on which the analytical equation of $R_{\mathrm{CO},90\%}$ is built. That being said, most substructures are found much closer to the star, far away from $R_{\mathrm{CO},90\%}$, meaning their effect on $R_{\mathrm{CO},90\%}$ is likely minimal.

Similarly, the temperature structure of the disk and its vertical structure or more precisely, how much of the CO column is frozen out, is a key link in the correlation of $N_{\mathrm{gas}}(R_{\mathrm{CO},90\%})$ and M_{gas}, as demonstrated by the tight correlation between $z_{\mathrm{freeze}}(R_{\mathrm{CO},90\%})$ and M_{gas}. We have explored the parameters that predominantly affect the temperature structure in our models. From the observational side, several recent studies have used high-resolution ALMA observations of CO to map the radial and vertical temperature structures of disks (e.g., Pinte et al. 2018; Law et al. 2021b, 2022; Paneque-Carreño et al. 2023). Temperature structures computed with models similar to the ones in this work have been found to match these observational constraints (e.g., Zhang et al. 2021). However, the number of disks with good observational constraints on their 2D temperature structures is still limited and, due to the requirement of deep, high-resolution observations, biased to large disks. There is therefore still the possibility that our models do not accurately describe the temperature structure of all disks, in which case it is very likely that the analytical expression for $R_{\mathrm{CO},90\%}$ presented in this work will no longer hold.

5. Conclusions

In this work we have presented an empirical relation between the gas column density measured at the observed gas outer

radius ($N_{gas}(R_{CO,90\%})$) and the mass of the disk M_{disk}. Using this relation we provided simple prescriptions for the conversions of R_c to $R_{CO,90\%}$ and from $R_{CO,90\%}$ to R_c (Equation (8)). Our main takeaway points are as follows:

1. Using thermochemical models, we found an empirical correlation between the gas column density at the observed gas disk size $R_{CO,90\%}$ and the mass of the disk:$N_{gas}(R_{CO,90\%}) \approx 3.7 \times 10^{21}(M_{disk}/M_\odot)^{0.34}$ cm^{-2}. Importantly, this correlation does not significantly depend on other disk parameters.

2. Following Toci et al. (2023) we used this empirical correlation to provide an analytical prescription of $R_{CO,90\%}$ that only depends on R_c and M_{disk}. This analytical prescription is able to reproduce $R_{CO,90\%}$ from thermochemical models for a large range of M_{disk} and R_c.

3. Exploring the analytical prescription of $R_{CO,90\%}$ reveals a maximum $R_{CO,90\%}$ for a given M_{disk} that is independent of R_c(Equation (11)). It also shows that for a given M_{disk} any $R_{CO,90\%}$ can be obtained with two different values of R_c ($R_c \ll R_{CO,90\%}$ or $R_c \gg R_{CO,90\%}$).

4. Using the observed $R_{CO,90\%}$ and $M_{gas} = 100 \times M_{dust}$ we derived R_c for four samples of disks in Lupus, Upper Sco, Taurus, and DSHARP. We find that Lupus and Taurus have similar median R_c, 19.8 and 20.9 au, respectively, and the DSHARP disks are slightly larger ($R_c = 26.1$). Surprisingly, the disks in Upper Sco are significantly smaller, with a median $R_c = 4.9$ au. This decrease in R_c for the older Upper Sco region goes against predictions of both viscous and wind-driven evolution.

Appendix A
A Toy Model for Analytically Deriving the Observed CO Outer Radius

Section 3.1 showed a clear correlation between the gas column density measured at $R_{CO,90\%}$, the radius that enclosed

---

9 http://www.astropy.org

90% of the ^{12}CO $J = 2$–1 emission, and the total mass of the disk M_{disk}. It also showed a similarly tight correlation between the height of the CO snow surface as measured at $R_{CO,90\%}$ and M_{disk}, giving a hint as to the origin of the first correlation. Here we will set up a simple toy model of the CO abundance in protoplanetary disks, link it to the resulting CO emission, and show how it can produce a correlation between the column density at the outer radius and the disk mass.

A.1. Concept and Assumptions

Starting from the observations, it is common to use ^{12}CO rotational emission to measure the size of protoplanetary disks. Low J lines of CO become optically thick already at small column densities, making CO emission bright and easy to detect out to large disk radii. The transition from optically thick to optically thin CO emission thus occurs in the outer part of the disk, where the surface density likely declines steeply with radius. This is indeed the case if the surface density follows an exponential taper, but one should keep in mind that observational constraints on the shape of the surface density in the outer disk are very limited (see, e.g., Cleeves et al. 2016; Dullemond et al. 2020). Given that the density is low here, we can expect only a small contribution of the optically thin CO emission to the total CO flux. In other words, we expect that most, if not all, of the CO emission is optically thick.

At the same time, we know that CO will become photodissociated in the outer disk. The exact CO column density required to self-shield against photodissociation depends somewhat on the molecular hydrogen column density and temperature, but in general the threshold is taken to be a CO column density of a few times 10^{15} cm^{-2} (see, e.g., van Dishoeck & Black 1988; Visser et al. 2009). It is common to assume that the radius at which the CO line emission becomes optically thin coincides with the radius at which CO stops being able to self-shield, i.e., that the CO emission disappears beyond this point (e.g., Trapman et al. 2019; Toci et al. 2023). In this case we can give a simple description of the CO radial emission profile of

$$I_{CO}(R) = \begin{cases} T_0\left(\dfrac{R}{R_0}\right)^{-\beta} & \text{if } N_{CO}(R) \geqslant a \times 10^{15} \text{ cm}^{-2}, \\ 0 & \text{otherwise,} \end{cases} \quad \text{(A1)}$$

where $T_0(R/R_0)^{-\beta}$ describes the temperature profile of the CO emitting layer as a simple power law and a is a constant of order unity.

Under the these simplifying assumptions, the radius that encloses 100% of the CO flux would be the radius where we reach $N_{CO}(R) \approx a \times 10^{15}$ cm^2. Note that the definition commonly used in observations to measure gas disk sizes, i.e., $R_{CO,90\%}$, the radius that encloses 90% of the flux, is very closely related to the 100% radius (see, e.g., Appendix F in Trapman et al. 2019):

$$R_{CO,100\%} = 0.9^{\frac{1}{(2-\beta)}}R_{CO,90\%}, \quad \text{(A2)}$$

$$\approx 0.93 \times R_{CO,90\%} \text{ for } \beta = 0.5. \quad \text{(A3)}$$

However, as we will discuss further on in this section, this small difference has a meaningful impact on the $N_{gas}(R_{CO,90\%})-M_{disk}$ relation discussed in the main body of this work. For the rest of the derivation we will therefore use $R_{CO,100\%} = R_{\tau_{CO}=1} \equiv R_\tau$ rather than $R_{CO,90\%}$.

The relation between the CO column density and the H_2 column density depends on the column-averaged CO abundance. The zeroth-order assumption would be that the CO abundance is a constant of 10^{-4}, where all of the available carbon is locked up in the gas. However, this ignores the fact that the disk becomes colder toward the midplane, causing the CO to freeze out and thus lowering the local CO abundance. Similarly, photodissociation will decrease the CO abundance in the uppermost layer of the disk. These two processes confine CO to a so-called warm molecular layer, first introduced as a concept by Aikawa et al. (2002). As a result, the column-averaged CO abundance will be lower than 10^{-4}.

Given that most of mass in the column is concentrated toward the midplane we can, to first order, ignore the decrease in CO abundance due to photodissociation and write the vertical CO abundance profile as a simple step function:

$$x_{CO}(R, z) = \begin{cases} 0 & \text{if } z \leqslant z_{freeze}(R), \\ x_{CO,peak} & \text{if } z > z_{freeze}(R), \end{cases} \quad (A4)$$

where $z_{freeze}(R)$ describes the height of the CO ice surface, which is approximately equivalent to $T_{gas}(R, z_{freeze}) = 20$ K and we assume that $x_{CO,peak} = 10^{-4}$.

In principle obtaining $z_{freeze}(R)$ requires computing the 2D temperature structure of the disk. This can be done by assuming that $T_{gas} \approx T_{dust}$, a reasonable assumption for the area of interest here, and computing $T_{dust}(r, z)$ by solving the radiative transfer equation (e.g., van der Tak et al. 2007; Brinch & Hogerheijde 2010; Dullemond et al. 2012). Alternatively, the temperature structure can be measured from optically thick emission lines (e.g., Dartois et al. 2003; Dullemond et al. 2020; Law et al. 2021b, 2022). Here we will keep using $z_{freeze}(R)$ until later in the derivation.

The vertical density distribution resulting from isothermal hydrostatic equilibrium is given by a Gaussian (e.g., Chiang & Goldreich 1997):

$$\rho_{gas} = \frac{\Sigma(r)}{\sqrt{2\pi}H(r)} \exp\left[-\frac{1}{2}\frac{z^2}{H(r)^2}\right], \quad (A5)$$

where $H(r)$ is the height of the disk.

To obtain the CO column density of our simple two-part CO abundance model (Equation (A4)) we need to find the column density above z_{freeze}:

$$N_{gas}(r) = \frac{\Sigma_{gas}(r)}{\mu m_H}, \quad (A6)$$

$$N_{>z_{fr}}(r) = \int_{z_{freeze}}^{\infty} \frac{\Sigma_{gas}(r)}{\mu m_H \sqrt{2\pi}H(r)} \exp\left[-\frac{1}{2}\frac{z^2}{H(r)^2}\right]dz, \quad (A7)$$

$$= N_{gas}(r)\frac{1}{\sqrt{2\pi}H(r)} \int_{z_{freeze}}^{\infty} \exp\left[-\frac{1}{2}\frac{z^2}{H(r)^2}\right]dz, \quad (A8)$$

$$\overset{t=z/\sqrt{2}H}{=} \frac{N_{gas}(r)}{\sqrt{\pi}} \int_{z_{freeze}/\sqrt{2}H}^{\infty} \exp[-t^2]dt, \quad (A9)$$

$$= \frac{N_{gas}(r)}{2}\left[1 - \text{erf}\left(\frac{z_{freeze}(r)}{\sqrt{2}H(r)}\right)\right]. \quad (A10)$$

Here N_{gas} is the gas column density, μ is the mean molecular weight, m_H is the hydrogen atomic mass, and erf is the error function. This allows us to write out the CO column density above z_{freeze} (see Equation (A4)) as

$$N_{CO} = x_{CO}N_{z>z_{freeze}} \quad (A11)$$

$$= \frac{x_{CO,peak}}{2}N_{gas}(r)\left[1 - \text{erf}\left(\frac{z_{freeze}(r)}{\sqrt{2}H(r)}\right)\right]. \quad (A12)$$

Using the gas surface density instead of the gas column density $N_{gas}(r)$, Equation (A11) becomes

$$\frac{2N_{CO}}{x_{CO,peak}} = \frac{\Sigma_{gas}(r)}{\mu m_H}\left[1 - \text{erf}\left(\frac{z_{freeze}(r)}{\sqrt{2}H(r)}\right)\right]. \quad (A13)$$

We recall that in our toy model R_τ coincides with the radius where the CO column density is the critical CO column density needed for CO self-shielding ($N_{CO}(R_\tau = N_{CO,crit})$). We can then derive an expression for R_τ from the previous equations as

$$\frac{2\mu m_H N_{CO}}{x_{CO,peak}} \equiv 2\Sigma_{CO,crit} = \Sigma_c\left[1 - \text{erf}\left(\frac{z_{freeze}(R_\tau)}{\sqrt{2}H(R_\tau)}\right)\right], \quad (A14)$$

$$\times \left(\frac{R_\tau}{R_c}\right)^{-\gamma+\xi}\exp\left[-\left(\frac{R_\tau}{R_c}\right)^{2-\gamma}\right], \quad (A15)$$

$$\frac{2\Sigma_{CO,crit}}{\Sigma_c} \equiv \hat{\Phi} = \left[1 - \text{erf}\left(\frac{z_{freeze}(R_\tau)}{\sqrt{2}H(R_\tau)}\right)\right], \quad (A16)$$

$$\times \left(\frac{R_\tau}{R_c}\right)^{-\gamma+\xi}\exp\left[-\left(\frac{R_\tau}{R_c}\right)^{2-\gamma}\right]. \quad (A17)$$

A solution for a similar equation without the CO freeze-out term in the square brackets was recently presented by Toci et al. (2023). Here we follow their work by introducing the shorthands $\Sigma_{CO,crit}$ and $\hat{\Phi}$.[10]

With the introduction of the CO freeze-out term Equation (A17) can no longer be solved analytically. However if the vertical density and temperature structure are known and prescriptions for $H(R_\tau)$ and $z_{freeze}(R_\tau)$, or more accurately $z_{freeze}(R_\tau)/H(R_\tau)$, can be provided the equation can be solved numerically.

As a proof-of-concept we obtain $z_{freeze}(R_\tau)$ from our models, in favor of the increased complexity that a full fit of the temperature structure would bring, and combine it with informed values of $x_{CO,peak} = 3 \times 10^{-5}$ and $N_{CO} = 3 \times 10^{15}$ cm^{-2} to calculate $N_{gas}(R_\tau)$ using Equation (A14). The left panel of Figure 8 shows that these analytical N_{gas} values reproduce the values from the models, including their dependence on disk mass. However, the figure also shows that the relation between $N_{gas}(R_\tau)$ and M_{disk} is not a power law as it is for $N_{gas}(R_{CO,90\%})$ and it is also less tight. The underlying cause for this is the fact that the relation between $R_{CO,90\%}$ and R_τ also depends on disk mass. The right panel of Figure 8 shows the ratio $R_\tau/R_{CO,90\%}$,

_____

[10] For direct comparison with Toci et al. (2023): $\Sigma_{crit,toci+2022} = \Sigma_{CO,crit}/[..]$ and $\Phi_{toci+2022} = 0.5\hat{\Phi}/[..]$, where $[..]$ is the term in square brackets in Equation (A14).
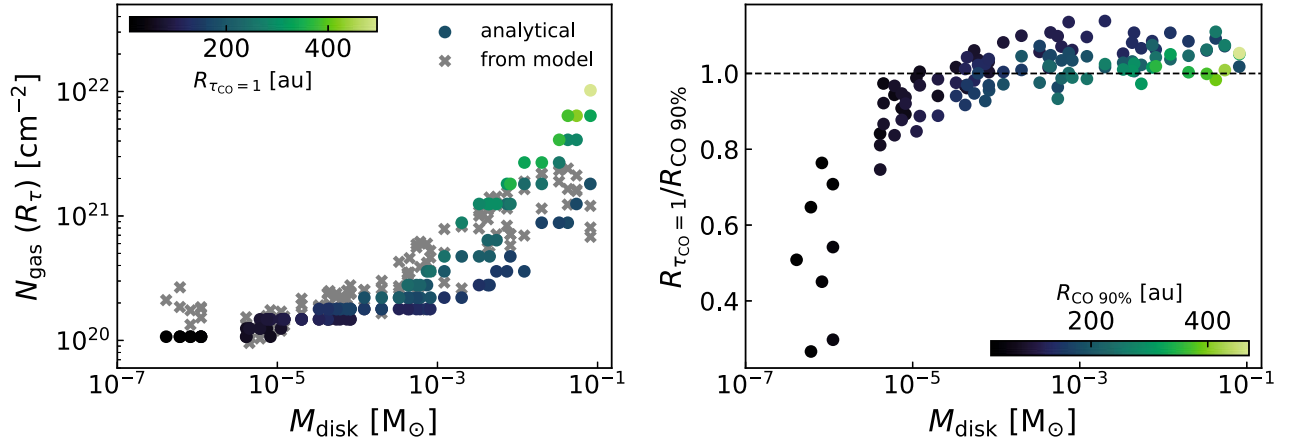
Figure 8. Left: comparison between $N_{\mathrm{gas}}(R_\tau)$ as derived from Equation (A12) and the value of $N_{\mathrm{gas}}(R_\tau)$ as obtained from the DALI models. For the analytical N_{gas}, $x_{\mathrm{CO,peak}} = 3 \times 10^{-5}$, $N_{\mathrm{CO}} = 3 \times 10^{15}\ \mathrm{cm}^{-2}$, and $z_{\mathrm{freeze}}(R_\tau)$ was also obtained from the models. Colors show the value of R_τ. Right: ratio of R_τ and $R_{\mathrm{CO,90\%}}$ set against the disk mass.

which decreases toward lower disk mass. This mass dependence might appear small, but one should bear in mind that the surface density at these radii follows an exponential; a small difference in radius will correspond to a much larger difference in the gas column density. This effect introduces a further mass dependence, as more massive disks have a larger $R_{\mathrm{CO,90\%}}$ (and R_τ) that lies further in the exponential taper of the surface density profile where it is steeper, meaning that differences between $R_{\mathrm{CO,90\%}}$ and R_τ will result in larger differences between $N_{\mathrm{gas}}(R_{\mathrm{CO,90\%}})$ and $N_{\mathrm{gas}}(R_\tau)$ for more massive disks. This is a complex process to model, prompting us to use the empirical correlation presented in Section 3.

Appendix B
Effect of the Disk and Stellar Parameters on the Height of the CO Snow Surface

In Figure 9 from left to right and top to bottom, the examined parameters are the stellar luminosity (L_*), the scale height at R_c (h_c), the external ISRF, the characteristic size (R_c), the slope of the surface density (γ), the disk flaring angle (ψ), the scale height reduction of the large grains (χ), and the fraction of large grains (f_{large}). The gray points in each panel show the fiducial models shown in Figure 1. The black dashed line shows $N_{\mathrm{gas}}(R_{\mathrm{CO,90\%}}) \propto M_{\mathrm{disk}}^{0.34}$.
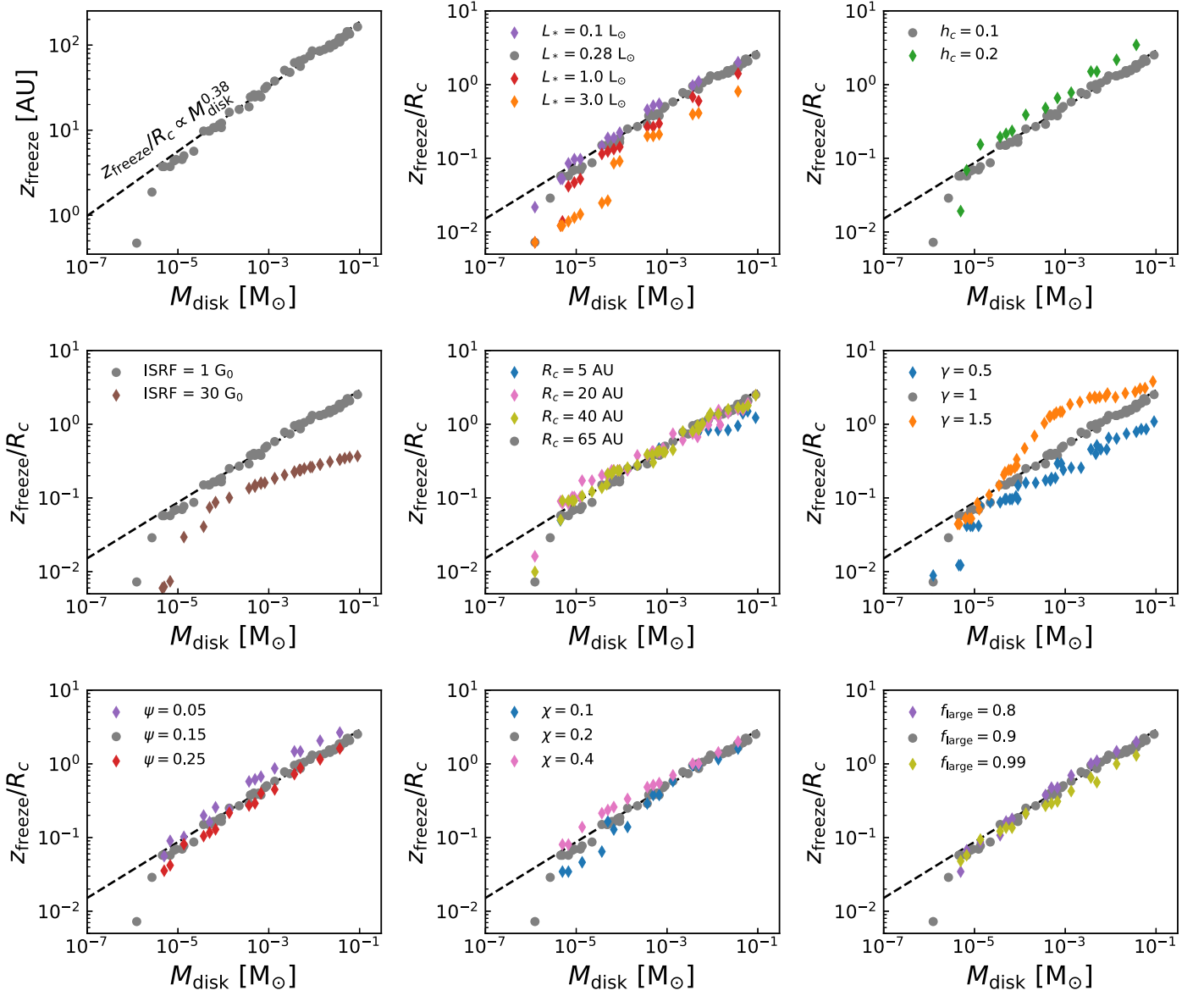
Figure 9. Height of the CO snow surface (z_{freeze}) at $R_{\text{CO},90\%}$ vs. disk mass. From left to right and top to bottom we show the effect of stellar luminosity (L_*), the scale height at R_c (h_c), the external ISRF, the characteristic size (R_c), the slope of the surface density (γ), the disk flaring angle (ψ), the scale height reduction of the large grains (χ), and the fraction of large grains (f_{large}). The gray points in each panel show the fiducial models shown in Figure 1. The black dashed line shows $z_{\text{freeze}}(R_{\text{CO},90\%})/R_c \propto M_{\text{disk}}^{0.38}$.

Appendix C
Measuring the Observed Disk Radius Using 68% Instead of 90% of the CO Flux

Throughout this work we have used $R_{CO,90\%}$ as an observational measure of the disk size, but tests show that a similar result, at least qualitatively, can also be obtained if we instead use the radius that encloses 68% of the CO 2–1 flux ($R_{CO,68\%}$). In Figure 10, we recreate Figure 1 but now for disk properties measured at $R_{CO,68\%}$, we find that there exists a similar power-law relation between $N_{gas}(R_{CO,68\%})$ and M_{disk} as there did for $R_{CO,90\%}$. While there is much less of a direct link between $R_{CO,68\%}$ and the radius where CO becomes photodissociated, a fact that can be gleaned from the wide range of N_{CO} at $R_{CO,68\%}$, we find a tight relation between $R_{CO,90\%}$ and $R_{CO,68\%}$ in our models which allows us to also relate $R_{CO,68\%}$ to the radius where CO becomes photodissociated. The tight relation between $R_{CO,90\%}$ and $R_{CO,68\%}$ reflects the overall similarity in CO emission profiles between our models, suggesting that our findings for $R_{CO,90\%}$ and $R_{CO,68\%}$ likely hold for most fraction-of-CO-flux radii.

If we fit a power law to $N_{gas}(R_{CO,68\%})$ and the disk mass we obtain the following critical gas column density:

$$N_{gas}(R_{CO,68\%}) \approx 4.1 \times 10^{22} \left(\frac{M_{gas}}{M_\odot}\right)^{0.5} \text{cm}^{-2}. \quad (C1)$$

Using this critical column density instead of the one for $R_{CO,90\%}$ changes the square bracket term in Equation (8) to

$$[..] = \frac{\Sigma_c}{\mu m_H N_{gas}(R_{CO,68\%})}, \quad (C2)$$

$$= 4.5 \times 10^6 \left(\frac{M_{disk}}{M_\odot}\right)^{0.5} \left(\frac{R_c}{\text{au}}\right)^{-2}, \quad (C3)$$

which gives us the following analytical prescription for $R_{CO,68\%}$:

$$R_{CO,68\%} = R_c \left(\frac{\gamma - \xi}{2 - \gamma} W\left(\frac{2 - \gamma}{\gamma - \xi}\left[4.5 \times 10^6 \left(\frac{M_d}{M_\odot}\right)^{0.5}\right.\right.\right.$$
$$\left.\left.\left. \times \left(\frac{R_c}{\text{au}}\right)^2\right]^{\frac{2-\gamma}{\gamma-\xi}}\right)\right)^{\frac{1}{2-\gamma}}. \quad (C4)$$
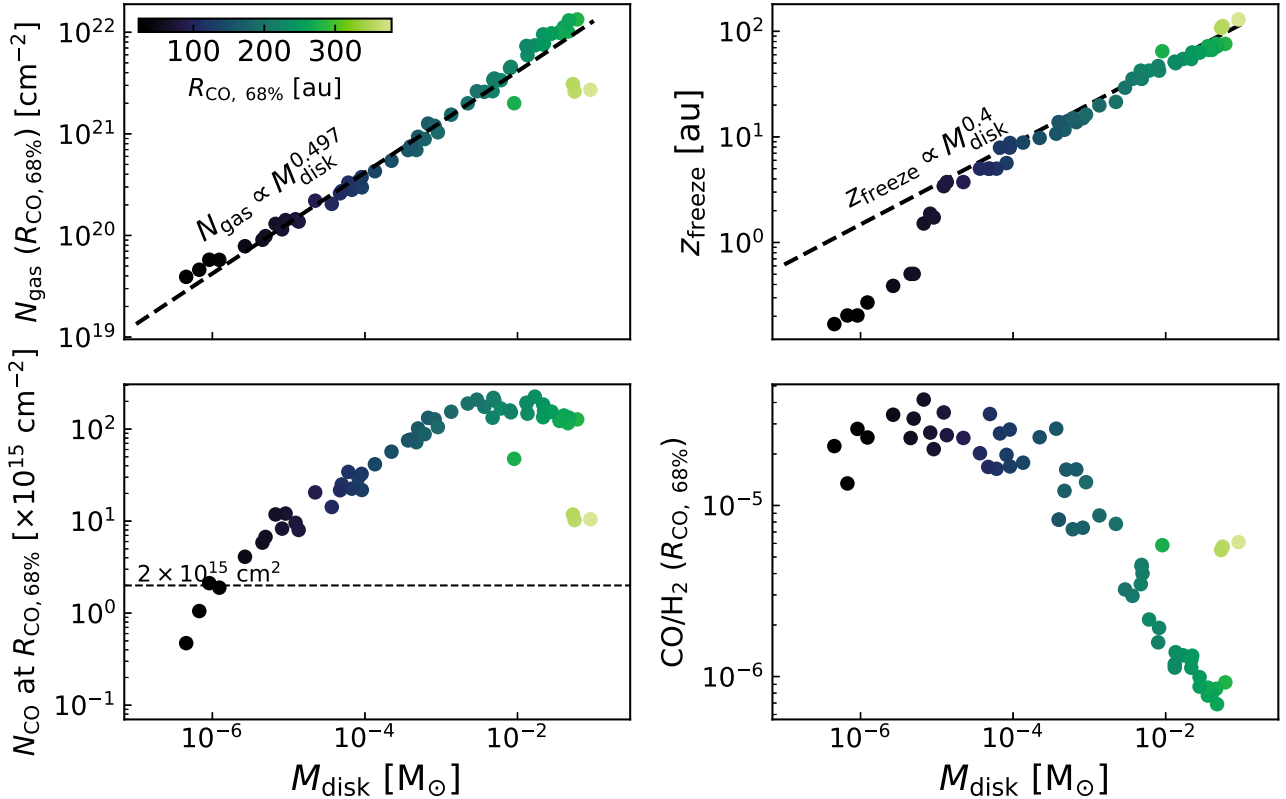

Figure 10. As Figure 1, but each property is now measured at the radius that encloses 68% of the CO emission.

Appendix D
Deriving a Minimum Disk Mass Based on $R_{\mathrm{CO},90\%}$

In Section 3.4 we showed that there is a minimum disk mass associated with each $R_{\mathrm{CO},90\%}$. Here we derive this mass analytically. We begin with the analytical formula for $R_{\mathrm{CO},90\%}$ (Equation (8)):

$$R_{\mathrm{CO},90\%} = R_c \left(\frac{\gamma - \xi}{2 - \gamma} W \left(\frac{2 - \gamma}{\gamma - \xi} \left[4.9 \cdot 10^7 \left(\frac{M_d}{M_\odot} \right)^{0.66} \right. \right. \right.$$
$$\left. \left. \left. \times \left(\frac{\mathrm{au}}{R_c} \right)^2 \right]^{\frac{2-\gamma}{\gamma-\xi}} \right) \right)^{\frac{1}{2-\gamma}}, \quad (D1)$$

$$= R_c \left[\frac{1}{a} W(x) \right]^{1/(2-\gamma)}. \quad (D2)$$

Here we have defined a few shorthands: $x = ay^a$, $y = 4.9 \cdot 10^7 \left(\frac{M_d}{M_\odot} \right)^{0.66} \left(\frac{R_c}{\mathrm{au}} \right)^{-2}$, and $a = \frac{2-\gamma}{\gamma-\xi}$. Taking the derivative of $R_{\mathrm{CO},90\%}$ to R_c and setting it to zero we obtain

$$\frac{\partial R_{\mathrm{CO},90\%}}{\partial R_c} = \left[\frac{1}{a} W(x) \right]^{1/(2-\gamma)} + R_c \frac{\partial}{\partial R_c} \left[\frac{1}{a} W(x) \right]^{1/(2-\gamma)}, \quad (D3)$$

$$= \left[\frac{1}{a} W(x) \right]^{\frac{1}{2-\gamma}} + \frac{R_c}{2-\gamma} \left[\frac{1}{a} W(x) \right]^{\frac{\gamma-1}{2-\gamma}} \frac{\partial W(x)}{\partial x} \frac{\partial x}{\partial y} \frac{\partial y}{\partial R_c}, \quad (D4)$$

$$= \left[\frac{1}{a} W(x) \right]^{\frac{1}{2-\gamma}} - 2 \frac{ax}{2-\gamma} \left[\frac{1}{a} W(x) \right]^{\frac{\gamma-1}{2-\gamma}} \frac{\partial W(x)}{\partial x}, \quad (D5)$$

$$= \left[\frac{1}{a} W(x) \right]^{\frac{1}{2-\gamma}} - 2 \frac{ax}{2-\gamma} \left[\frac{1}{a} W(x) \right]^{\frac{\gamma-1}{2-\gamma}} \frac{W(x)}{x(1 + W(x))}, \quad (D6)$$

$$0 = 1 - \frac{2a}{2-\gamma} \left[\frac{1}{a} W(x) \right]^{-1} \frac{W(x)}{(1 + W(x))}, \quad (D7)$$

$$\frac{2-\gamma}{2a^2} = \frac{1}{(1 + W(x))}, \quad (D8)$$

$$W(x) = \frac{2a^2}{2-\gamma} - 1. \quad (D9)$$

The inverse Lambert W-function is given by $W^{-1}(y) = ye^y$. With this and our shorthands we can write out the maximum $R_{\mathrm{CO},90\%}$, and its corresponding R_c, for a given mass M_{disk} as

$$R_{c,\mathrm{max}} = \sqrt{4.9 \cdot 10^7 M_{\mathrm{disk}}^{0.66} \left[\frac{1}{a} W^{-1} \left(\frac{2a^2}{2-\gamma} - 1 \right) \right]^{-\frac{1}{2a}}}, \quad (D10)$$

$$R_{\mathrm{CO},90\%,\mathrm{max}} = R_{c,\mathrm{max}} \left[\frac{1}{a} \left(\frac{2a^2}{2-\gamma} - 1 \right) \right]^{1/(2-\gamma)}. \quad (D11)$$

For $\gamma = 1$, $\xi = 0$ these equations reduce to

$$R_{\mathrm{CO},90\%,\mathrm{max}} = R_{c,\mathrm{max}} = \sqrt{\frac{4.9 \cdot 10^7 M_{\mathrm{disk}}^{0.66}}{e}}. \quad (D12)$$

Writing the disk mass in terms of $R_{\mathrm{CO},90\%,\mathrm{max}}$ then gives Equation (11):

$$M_{\mathrm{disk}}$$
$$\geqslant \left[\frac{e R_{\mathrm{CO},90\%,\mathrm{max}}}{4.9 \cdot 10^7} \right]^{1/0.66} \gtrsim 1.295 \times 10^{-5} \left(\frac{R_{\mathrm{CO},90\%}}{100 \ \mathrm{au}} \right)^3 M_\odot. \quad (D13)$$

Appendix E
Deriving R_c for Disks in Lupus, Upper Sco, Taurus, and DSHARP

Our approach for deriving R_c is as follows (shown in Figure 11). We collected a sample of disks with a measured $R_{\mathrm{CO},90\%}$ or an upper limit on $R_{\mathrm{CO},90\%}$ from the literature (Barenfeld et al. 2017; Ansdell et al. 2018; Sanchis et al. 2021; Long et al. 2022; see Table 2). For each source in this sample we first draw a random $M_{\mathrm{disk}} = 100 \times M_{\mathrm{dust}}$ from the distribution of the observed M_{dust} and its uncertainties. We do the same for $R_{\mathrm{CO},90\%}$, where the upper limits on $R_{\mathrm{CO},90\%}$ are treated as a uniform distribution between 0 and the upper limit. For Upper Sco $R_{\mathrm{CO},90\%}$ is calculated from fitted CO intensity profile reported in Table 4 in Barenfeld et al. (2017). Note that the uncertainties on the intensity profile are asymmetrical, which when propagated into the uncertainty on $R_{\mathrm{CO},90\%}$ is represented by a two half-Gaussians with different widths (see Figure 12). For this $(M_{\mathrm{disk}}, R_{\mathrm{CO},90\%})_i$, we calculate R_c by inverting Equation (8), where we assume that $R_{\mathrm{CO},90\%} \gg R_c$ (see Section 3.4). This procedure is repeated $N = 1000$ times to sample the distribution of R_c of each source properly. Tables 2 and 3 list the derived R_c and its uncertainties for each source.
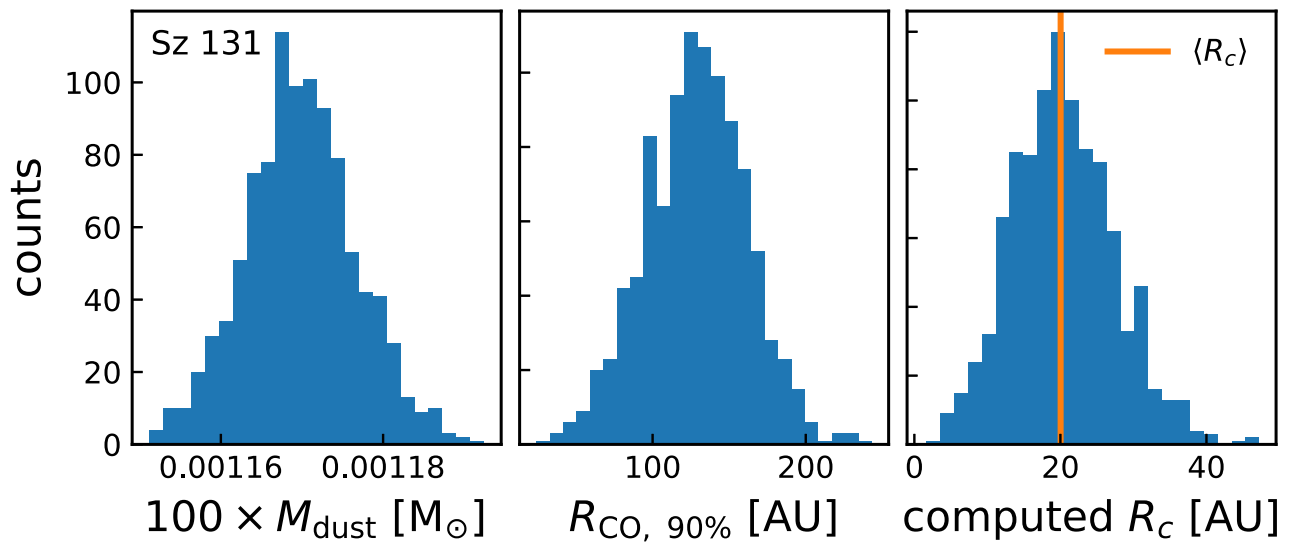
Figure 11. Example of how R_c is derived. A total of 1000 samples is drawn from the dust mass M_{dust} and observed gas disk size $R_{CO,90\%}$ of Sz 131 based on the Gaussian uncertainties found for these two properties (leftmost and center panels). These samples ($100 \times M_{dust}$, $R_{CO,90\%}$) are then used to calculate the corresponding $R_{c,i}$, resulting the distribution of R_c shown in the rightmost panel.
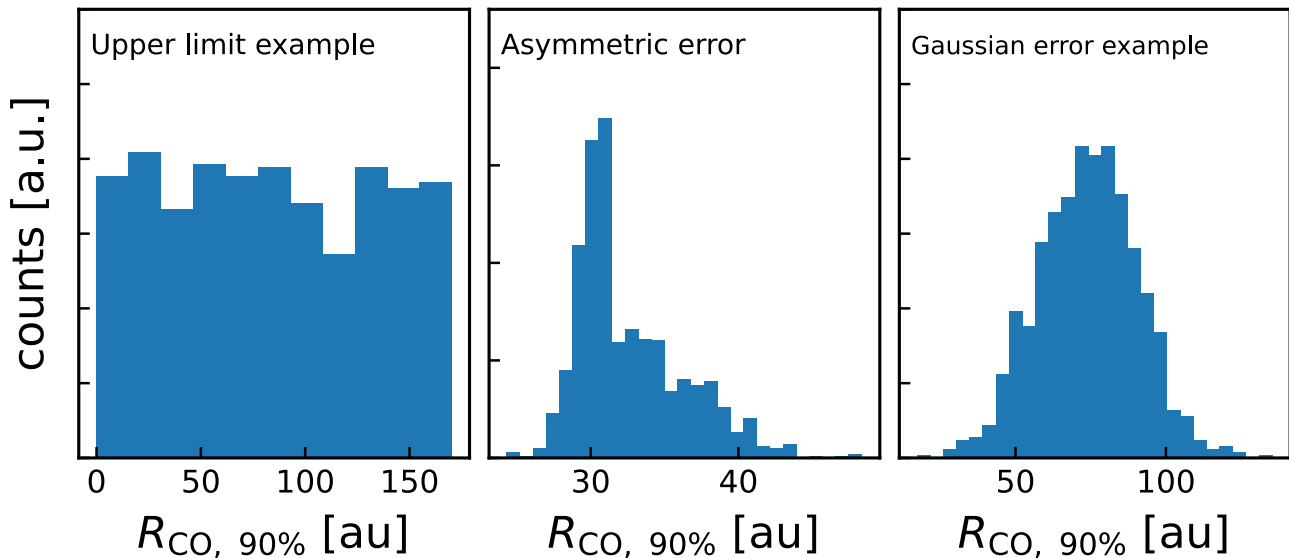
Figure 12. Examples of the three types of uncertainties on $R_{CO,90\%}$ in our sample. Left: upper limits on $R_{CO,90\%}$ are represented by a uniform distribution between 0 and the upper limit. Middle: the asymmetrical uncertainties on $R_{CO,90\%}$ in Upper Sco are represented by two half-Gaussians with different widths. Right: for the majority of sources the uncertainties on $R_{CO,90\%}$ follow a Gaussian distribution.

Table 2
Derived R_c for Lupus, Upper Sco, Taurus, and DSHARP

Name	Sample	M_{dust} ($M_\oplus$)	$R_{CO,90\%}$ (au)	R_c (au)	References
EX Lup	Lupus	19.1 ± 0.4	$\leqslant 170.3$	$3.8^{+6.0}_{-5.4}$	(2, 3, 4)
Lup706	Lupus	0.4 ± 0.0	$\leqslant 87.2$	$2.6^{+6.1}_{-4.0}$	(1, 3, 4)
RXJ1556.1-3655	Lupus	24.8 ± 0.1	118.5 ± 11.2	$13.1^{+1.1}_{-1.2}$	(2, 3, 4)
RY Lup	Lupus	123.0 ± 0.3	323.0 ± 96.9	$29.7^{+12.5}_{-10.2}$	(1, 3, 4)
Sz 65	Lupus	27.4 ± 0.1	167.7 ± 19.9	$18.5^{+2.3}_{-2.3}$	(1, 3, 4)
Sz 66	Lupus	6.5 ± 0.1	$\leqslant 135.3$	$3.4^{+5.4}_{-4.6}$	(1, 3, 4)
Sz 69	Lupus	7.1 ± 0.1	123.7 ± 17.6	$15.9^{+2.7}_{-2.2}$	(1, 3, 4)
Sz 72	Lupus	6.0 ± 0.1	32.7 ± 11.1	$2.3^{+0.9}_{-0.8}$	(1, 3, 4)
Sz 73	Lupus	13.2 ± 0.1	106.6 ± 13.3	$11.5^{+1.4}_{-1.3}$	(1, 3, 4)
Sz 75	Lupus	31.9 ± 0.1	226.2 ± 67.9	$22.1^{+7.1}_{-7.8}$	(1, 3, 4)
Sz 76	Lupus	4.9 ± 0.2	140.4 ± 13.6	$19.7^{+2.1}_{-1.9}$	(2, 3, 4)
Sz 77	Lupus	2.1 ± 0.1	37.2 ± 17.6	$2.4^{+1.6}_{-1.6}$	(2, 3, 4)
Sz 83	Lupus	191.7 ± 0.2	$\leqslant 347.9$	$7.9^{+11.5}_{-10.3}$	(1, 3, 4)
Sz 84	Lupus	13.4 ± 0.1	192.3 ± 25.9	$26.8^{+3.9}_{-3.4}$	(1, 3, 4)
Sz 90	Lupus	9.9 ± 0.2	75.4 ± 22.8	$6.5^{+2.2}_{-2.1}$	(1, 3, 4)
Sz 91	Lupus	27.7 ± 0.5	330.9 ± 99.3	$40.4^{+17.7}_{-16.4}$	(1, 3, 4)
Sz 96	Lupus	1.8 ± 0.1	32.9 ± 15.5	$2.2^{+1.3}_{-1.3}$	(1, 3, 4)
Sz 100	Lupus	18.1 ± 0.2	128.7 ± 23.3	$14.6^{+2.9}_{-2.6}$	(1, 3, 4)
Sz 102	Lupus	6.1 ± 0.4	74.5 ± 45.0	$6.2^{+6.2}_{-4.9}$	(2, 3, 4)
Sz 111	Lupus	79.3 ± 0.4	459.1 ± 137.7	$56.2^{+24.6}_{-22.8}$	(1, 3, 4)
Sz 114	Lupus	44.8 ± 0.2	170.3 ± 34.5	$18.2^{+3.7}_{-3.6}$	(1, 3, 4)
Sz 118	Lupus	30.0 ± 0.4	145.9 ± 32.6	$14.4^{+3.7}_{-2.8}$	(1, 3, 4)
Sz 130	Lupus	2.8 ± 0.1	120.2 ± 27.3	$15.3^{+4.4}_{-3.5}$	(1, 3, 4)
Sz 131	Lupus	3.9 ± 0.1	128.2 ± 34.1	$15.3^{+5.1}_{-4.7}$	(1, 3, 4)
Sz 133	Lupus	28.5 ± 0.2	206.7 ± 23.9	$28.1^{+3.8}_{-3.8}$	(1, 3, 4)
J154518.5-342125	Lupus	2.3 ± 0.2	36.4 ± 12.9	$3.0^{+1.4}_{-1.2}$	(1, 3, 4)
J160002.4-422216	Lupus	57.0 ± 0.1	261.1 ± 30.4	$34.0^{+3.8}_{-4.5}$	(1, 3, 4)
J160703.9-391112	Lupus	2.0 ± 0.2	225.1 ± 67.5	$51.6^{+57.4}_{-30.1}$	(1, 3, 4)
J160830.7-382827	Lupus	58.2 ± 0.5	343.4 ± 103.0	$34.6^{+14.2}_{-12.3}$	(1, 3, 4)
J160901.4-392512	Lupus	8.3 ± 0.3	193.9 ± 18.7	$30.3^{+3.0}_{-3.2}$	(1, 3, 4)
J160927.0-383628	Lupus	1.7 ± 0.1	113.1 ± 20.4	$16.1^{+3.2}_{-3.1}$	(1, 3, 4)
J161029.6-392215	Lupus	3.4 ± 0.1	133.8 ± 25.5	$18.0^{+4.3}_{-3.8}$	(1, 3, 4)
J161243.8-381503	Lupus	13.5 ± 0.2	67.1 ± 24.9	$4.9^{+2.3}_{-2.3}$	(1, 3, 4)
V1094Sco	Lupus	230.3 ± 8.4	420.9 ± 32.7	$50.6^{+3.5}_{-3.9}$	(2, 3, 4)
V1192Sco	Lupus	0.4 ± 0.1	$\leqslant 226.2$	$8.1^{+21.6}_{-15.0}$	(1, 3, 4)
J16070854-3914075	Lupus	50.2 ± 0.6	339.3 ± 47.5	$45.4^{+8.1}_{-6.9}$	(1, 3, 4)

....

References. (1) Ansdell et al. (2018), (2) Ansdell et al. (2016), (3) Sanchis et al. (2021), (4) Alcalá et al. (2019), (5) Barenfeld et al. (2016), (6) Barenfeld et al. (2017), (7) Facchini et al. (2019), (8) Long et al. (2018), (9) Flaherty et al. (2020), (10) Pegues et al. (2021), (11) Kurtovic et al. (2021), (12) Long et al. (2022), and (13) Andrews et al. (2018).

Table 3
Derived R_c for Lupus, Upper Sco, Taurus, and DSHARP, cont'd

Name	Sample	$M_{\rm dust}$ ($M_\oplus$)	$R_{\rm CO,90\%}$ (au)	R_c (au)	References
....					
J16081497-3857145	Lupus	3.7 ± 0.1	95.1 ± 31.5	$10.9^{+5.5}_{-4.9}$	(1, 3, 4)
J16085953-3856275	Lupus	0.2 ± 0.0	$\leqslant 36.0$	$0.8^{+1.5}_{-1.3}$	(1, 3, 4)
CX Tau	Taurus	4.8 ± 0.5	115.0 ± 13.0	$14.8^{+1.4}_{-1.7}$	(7, 12)
DL Tau	Taurus	130.1 ± 13.0	597.0 ± 91.0	$82.8^{+14.9}_{-13.3}$	(8, 12)
DM Tau	Taurus	49.9 ± 5.0	876.0 ± 23.0	$246.6^{+9.2}_{-13.2}$	(12)
GO Tau	Taurus	34.2 ± 3.4	1014.0 ± 83.0	$325.5^{+54.7}_{-42.0}$	(8, 12)
UZ Tau	Taurus	67.0 ± 6.7	389.0 ± 75.0	$47.2^{+10.7}_{-9.8}$	(8, 12)
FP Tau	Taurus	4.1 ± 0.4	74.0 ± 17.0	$7.8^{+1.8}_{-1.7}$	(10, 12)
CIDA1	Taurus	13.3 ± 1.3	132.0 ± 14.0	$16.2^{+1.8}_{-1.7}$	(11, 12)
CIDA7	Taurus	9.5 ± 0.9	95.0 ± 11.0	$11.1^{+1.3}_{-1.3}$	(11, 12)
MHO6	Taurus	19.8 ± 2.0	218.0 ± 7.0	$35.2^{+1.2}_{-0.9}$	(11, 12)
J0415	Taurus	0.4 ± 0.0	47.0 ± 13.0	$5.1^{+1.6}_{-1.8}$	(11, 12)
J0420	Taurus	9.6 ± 1.0	59.0 ± 10.0	$5.8^{+1.0}_{-0.9}$	(11, 12)
J0433	Taurus	22.5 ± 2.3	165.0 ± 12.0	$21.7^{+1.5}_{-1.7}$	(11, 12)
GW Lup	DSHARP	60.5 ± 6.1	267.0 ± 8.0	$36.2^{+1.1}_{-1.0}$	(13, 12)
IM Lup	DSHARP	178.8 ± 17.9	803.0 ± 9.0	$123.2^{+0.0}_{-2.2}$	(13, 12)
MY Lup	DSHARP	54.4 ± 5.4	192.0 ± 7.0	$18.3^{+1.9}_{-2.3}$	(13, 12)
Sz 129	DSHARP	63.1 ± 6.3	130.0 ± 8.0	$16.5^{+3.5}_{-3.5}$	(13, 12)
AS 209	DSHARP	119.4 ± 11.9	280.0 ± 5.0	$33.1^{+0.6}_{-0.6}$	(13, 12)
SR4	DSHARP	35.1 ± 3.5	82.0 ± 7.0	$7.5^{+0.6}_{-0.6}$	(13, 12)
DoAr25	DSHARP	132.7 ± 13.3	233.0 ± 6.0	$26.4^{+0.7}_{-0.5}$	(13, 12)
DoAr33	DSHARP	19.1 ± 1.9	64.0 ± 6.0	$5.7^{+0.5}_{-0.5}$	(13, 12)
WaOph6	DSHARP	69.0 ± 6.9	297.0 ± 7.0	$36.2^{+0.7}_{-0.9}$	(13, 12)
HD142666	DSHARP	74.4 ± 7.4	171.0 ± 5.0	$16.8^{+0.4}_{-0.4}$	(13, 12)
HD143006	DSHARP	45.5 ± 4.5	154.0 ± 5.0	$16.0^{+0.5}_{-0.4}$	(13, 12)
HD163296	DSHARP	206.5 ± 20.7	478.0 ± 5.0	$54.1^{+0.3}_{-0.6}$	(13, 12)

References. (1) Ansdell et al. (2018), (2) Ansdell et al. (2016), (3) Sanchis et al. (2021), (4) Alcalá et al. (2019), (5) Barenfeld et al. (2016), (6) Barenfeld et al. (2017), (7) Facchini et al. (2019), (8) Long et al. (2018), (9) Flaherty et al. (2020), (10) Pegues et al. (2021), (11) Kurtovic et al. (2021), (12) Long et al. (2022), and (13) Andrews et al. (2018).

ORCID iDs

Leon Trapman ⓘ https://orcid.org/0000-0002-8623-9703
Giovanni Rosotti ⓘ https://orcid.org/0000-0003-4853-5736
Ke Zhang ⓘ https://orcid.org/0000-0002-0661-7517
Benoît Tabone ⓘ https://orcid.org/0000-0002-1103-3225

References

Aikawa, Y., van Zadelhoff, G., van Dishoeck, E. F., & Herbst, E. 2002, A&A, 386, 622
Alcalá, J. M., Manara, C. F., France, K., et al. 2019, A&A, 629, A108
Alessi, M., & Pudritz, R. E. 2022, MNRAS, 515, 2548
Anderson, D. E., Blake, G. A., Bergin, E. A., et al. 2019, ApJ, 881, 127
Andrews, S. M., Terrell, M., Tripathi, A., et al. 2018, ApJ, 865, 157
Andrews, S. M., Wilner, D. J., Espaillat, C., et al. 2011, ApJ, 732, 42
Ansdell, M., Williams, J. P., Manara, C. F., et al. 2017, AJ, 153, 240
Ansdell, M., Williams, J. P., Trapman, L., et al. 2018, ApJ, 859, 21
Ansdell, M., Williams, J. P., van der Marel, N., et al. 2016, ApJ, 828, 46
Armitage, P. J., Simon, J. B., & Martin, R. G. 2013, ApJL, 778, L14
Artymowicz, P., & Lubow, S. H. 1994, ApJ, 421, 651
Astropy Collaboration, Price-Whelan, A. M., Sipőcz, B. M., et al. 2018, AJ, 156, 123
Astropy Collaboration, Robitaille, T. P., Tollerud, E. J., et al. 2013, A&A, 558, A33
Avenhaus, H., Quanz, S. P., Garufi, A., et al. 2018, ApJ, 863, 44
Bai, X.-N. 2016, ApJ, 821, 80
Barenfeld, S. A., Carpenter, J. M., Ricci, L., & Isella, A. 2016, ApJ, 827, 142
Barenfeld, S. A., Carpenter, J. M., Sargent, A. I., et al. 2019, ApJ, 878, 45

Barenfeld, S. A., Carpenter, J. M., Sargent, A. I., Isella, A., & Ricci, L. 2017, ApJ, 851, 85
Birnstiel, T., Klahr, H., & Ercolano, B. 2012, A&A, 539, A148
Bosman, A. D., Walsh, C., & van Dishoeck, E. F. 2018, A&A, 618, A182
Brinch, C., & Hogerheijde, M. R. 2010, A&A, 523, A25
Bruderer, S. 2013, A&A, 559, A46
Bruderer, S., van Dishoeck, E. F., Doty, S. D., & Herczeg, G. J. 2012, A&A, 541, A91
Cardelli, J. A., Meyer, D. M., Jura, M., & Savage, B. D. 1996, ApJ, 467, 334
Chiang, E. I., & Goldreich, P. 1997, ApJ, 490, 368
Clarke, C. J. 2007, MNRAS, 376, 1350
Cleeves, L. I., Öberg, K. I., Wilner, D. J., et al. 2016, ApJ, 832, 110
Comerón, F. 2008, in Handbook of Star Forming Regions, Vol. 2, ed. B. Reipurth (San Francisco, CA: ASP), 295
Corless, R. M., Gonnet, G. H., Hare, D. E., Jeffrey, D. J., & Knuth, D. E. 1996, Advances in Computational Mathematics, 5, 329
Dartois, E., Dutrey, A., & Guilloteau, S. 2003, A&A, 399, 773
Dullemond, C. P., & Dominik, C. 2004, A&A, 417, 159
Dullemond, C. P., Isella, A., Andrews, S. M., Skobleva, I., & Dzyurkevich, N. 2020, A&A, 633, A137
Dullemond, C. P., Juhasz, A., Pohl, A., et al. 2012, RADMC-3D: A Multi-purpose Radiative Transfer Tool, Astrophysics Source Code Library, ascl:1202.015
Facchini, S., Birnstiel, T., Bruderer, S., & van Dishoeck, E. F. 2017, A&A, 605, A16
Facchini, S., Clarke, C. J., & Bisbas, T. G. 2016, MNRAS, 457, 3593
Facchini, S., van Dishoeck, E. F., Manara, C. F., et al. 2019, A&A, 626, L2
Favre, C., Cleeves, L. I., Bergin, E. A., Qi, C., & Blake, G. A. 2013, ApJL, 776, L38
Ferreira, J. 1997, A&A, 319, 340

Ferreira, J., & Pelletier, G. 1995, A&A, 295, 807
Flaherty, K., Hughes, A. M., Simon, J. B., et al. 2020, ApJ, 895, 109
Hartmann, L., Calvet, N., Gullbring, E., & D'Alessio, P. 1998, ApJ, 495, 385
Haworth, T. J., Clarke, C. J., Rahman, W., Winter, A. J., & Facchini, S. 2018, MNRAS, 481, 452
Haworth, T. J., Facchini, S., Clarke, C. J., & Cleeves, L. I. 2017, MNRAS Lett., 468, L108
Hendler, N., Pascucci, I., Pinilla, P., et al. 2020, ApJ, 895, 126
Hunter, J. D. 2007, CSE, 9, 90
Jonkheid, B., Dullemond, C. P., Hogerheijde, M. R., & van Dishoeck, E. F. 2007, A&A, 463, 203
Kama, M., Bruderer, S., van Dishoeck, E. F., et al. 2016, A&A, 592, A83
Kama, M., Folsom, C. P., & Pinilla, P. 2015, A&A, 582, L10
Kraus, A. L., Ireland, M. J., Hillenbrand, L. A., & Martinache, F. 2012, ApJ, 745, 19
Krijt, S., Bosman, A. D., Zhang, K., et al. 2020, ApJ, 899, 134
Krijt, S., Schwarz, K. R., Bergin, E. A., & Ciesla, F. J. 2018, ApJ, 864, 78
Kurtovic, N. T., Pinilla, P., Long, F., et al. 2021, A&A, 645, A139
Law, C. J., Crystian, S., Teague, R., et al. 2022, ApJ, 932, 114
Law, C. J., Loomis, R. A., Teague, R., et al. 2021a, ApJS, 257, 3
Law, C. J., Teague, R., Loomis, R. A., et al. 2021b, ApJS, 257, 4
Lee, H. H., Herbst, E., Pineau des Forets, G., Roueff, E., & Le Bourlot, J. 1996, A&A, 311, 690
Long, F., Andrews, S. M., Rosotti, G., et al. 2022, ApJ, 931, 6
Long, F., Herczeg, G. J., Pascucci, I., et al. 2017, ApJ, 844, 99
Long, F., Pinilla, P., Herczeg, G. J., et al. 2018, ApJ, 869, 17
Lynden-Bell, D., & Pringle, J. E. 1974, MNRAS, 168, 603
Manara, C. F., Ansdell, M., Rosotti, G. P., et al. 2023, in ASP Conf. Ser. 534, Protostars and Planets VII, ed. S-i Inutsuka et al. (San Francisco, CA: ASP)
Miotello, A., van Dishoeck, E., Williams, J., et al. 2017, A&A, 599, A113
Morbidelli, A., & Raymond, S. N. 2016, JGRE, 121, 1962
Paneque-Carreño, T., Miotello, A., van Dishoeck, E. F., et al. 2023, A&A, 669, A126
Papaloizou, J., & Pringle, J. E. 1977, MNRAS, 181, 441
Pecaut, M. J., Mamajek, E. E., & Bubar, E. J. 2012, ApJ, 746, 154
Pegues, J., Öberg, K. I., Bergner, J. B., et al. 2021, ApJ, 911, 150
Pinilla, P., Pascucci, I., & Marino, S. 2020, A&A, 635, A105
Pinte, C., Ménard, F., Duchêne, G., et al. 2018, A&A, 609, A47
Preibisch, T., Brown, A. G. A., Bridges, T., Guenther, E., & Zinnecker, H. 2002, AJ, 124, 404
Rosotti, G. P., & Clarke, C. J. 2018, MNRAS, 473, 5630
Rosotti, G. P., Tazzari, M., Booth, R. A., et al. 2019, MNRAS, 486, 4829
Sanchis, E., Testi, L., Natta, A., et al. 2021, A&A, 649, A19
Schwarz, K. R., Bergin, E. A., Cleeves, L. I., et al. 2016, ApJ, 823, 91
Schwarz, K. R., Calahan, J. K., Zhang, K., et al. 2021, ApJS, 257, 20
Sellek, A. D., Booth, R. A., & Clarke, C. J. 2020, MNRAS, 492, 1279
Tabone, B., Rosotti, G. P., Cridland, A. J., Armitage, P. J., & Lodato, G. 2022, MNRAS, 512, 2290
Tazzari, M., Clarke, C. J., Testi, L., et al. 2021, MNRAS, 506, 2804
Toci, C., Lodato, G., Livio, F. G., Rosotti, G., & Trapman, L. 2023, MNRAS Lett., 518, L69
Trapman, L., Facchini, S., Hogerheijde, M. R., van Dishoeck, E. F., & Bruderer, S. 2019, A&A, 629, A79
Trapman, L., Rosotti, G., Bosman, A. D., Hogerheijde, M. R., & van Dishoeck, E. F. 2020, A&A, 640, A5
Trapman, L., Tabone, B., Rosotti, G., & Zhang, K. 2022a, ApJ, 926, 61
Trapman, L., Zhang, K., van 't Hoff, M. L. R., Hogerheijde, M. R., & Bergin, E. A. 2022b, ApJL, 926, L2
Tripathi, A., Andrews, S. M., Birnstiel, T., & Wilner, D. J. 2017, ApJ, 845, 44
van der Tak, F. F. S., Black, J. H., Schöier, F. L., Jansen, D. J., & van Dishoeck, E. F. 2007, A&A, 468, 627
van Dishoeck, E. F., & Black, J. H. 1988, ApJ, 334, 771
Vicente, S. M., & Alves, J. 2005, A&A, 441, 195
Virtanen, P., Gommers, R., Oliphant, T. E., et al. 2020, NatMe, 17, 261
Visser, R., van Dishoeck, E. F., & Black, J. H. 2009, A&A, 503, 323
Weidenschilling, S. J. 1977, MNRAS, 180, 57
Weingartner, J. C., & Draine, B. 2001, ApJ, 548, 296
Williams, J. P., & Cieza, L. A. 2011, ARA&A, 49, 67
Winter, A. J., Clarke, C. J., Rosotti, G., et al. 2018, MNRAS, 478, 2700
Winter, A. J., & Haworth, T. J. 2022, EPJP, 137, 1132
Woitke, P., Kamp, I., & Thi, W.-F. 2009, A&A, 501, 383
Yang, H., & Bai, X.-N. 2021, ApJ, 922, 201
Yu, M., Evans, & Neal, J. 2017, ApJ, 841, 39
Zagaria, F., Clarke, C. J., Rosotti, G. P., & Manara, C. F. 2022, MNRAS, 512, 3538
Zagaria, F., Facchini, S., Miotello, A., et al. 2023a, A&A, 672, L15
Zagaria, F., Rosotti, G. P., Alexander, R. D., & Clarke, C. J. 2023b, EPJP, 138, 25
Zagaria, F., Rosotti, G. P., & Lodato, G. 2021, MNRAS, 504, 2235
Zhang, K., Bergin, E. A., Schwarz, K., Krijt, S., & Ciesla, F. 2019, ApJ, 883, 98
Zhang, K., Booth, A. S., Law, C. J., et al. 2021, ApJS, 257, 5
Zhang, K., Schwarz, K. R., & Bergin, E. A. 2020, ApJL, 891, L17
Zurlo, A., Cieza, L. A., Ansdell, M., et al. 2021, MNRAS, 501, 2305